An imaging method to measure conformational changes of voltage sensors of endogenous ion channels in tissue

Authors

Parashar Thapa[1‡], Robert Stewart[1‡], Rebecka J. Sepela[1], Oscar Vivas[2], Laxmi K. Parajuli[2], Mark Lillya[1], Sebastian Fletcher-Taylor[1], Bruce E. Cohen[3], Karen Zito[2], Jon T. Sack[1*]

[1]Department of Physiology and Membrane Biology, University of California, Davis, CA 95616
[2]Center for Neuroscience, University of California, Davis, CA 95616
[3]Molecular Foundry, Lawrence Berkeley National Laboratory, Berkeley, CA 94720

‡Authors contributed equally to this work
*Correspondence to jsack@ucdavis.edu

Abstract

A primary goal of molecular physiology is to understand the coupling between protein conformational change and systemic function. To see the conformational changes of a voltage-sensing protein within tissue, we synthesized a fluorescent molecular probe compatible with two-photon microscopy and developed a method to deconvolve conformational changes from fluorescence images. The probe was a fluorescently-tagged variant of a tarantula venom peptide that binds Kv2-type voltage gated K^+ channel proteins when their voltage-sensing domains are in a resting conformation. Kv2 proteins in cell membranes were labeled by the probe, and the intensity of labeling responded to voltage changes. Voltage-response characteristics were used to calibrate a statistical thermodynamic model relating labeling intensity to the conformations adopted by unlabeled voltage sensors. Two-photon imaging of rat brain slices revealed fluorescence consistent with conformation-selective labeling of endogenous neuronal Kv2 proteins. In principle, this method of deconvolving images into measures of protein conformational change is generalizable to other proteins labeled with conformation-selective probes.

Introduction

Proteins are dynamic, alternately settling into a few energetically favorable spatial arrangements, or conformations. Proteins respond to changes in their environment by changing their conformation. In response to changes in voltage across a cell membrane, ion channel voltage sensor domains change conformation (Zheng and Trudeau, 2016). These conformational changes are the initiating steps of a systemic physiological response to the voltage change. We have previously reported the synthesis and mechanistic validation of exogenous probes that fluorescently label ion channels voltage sensors in a conformational-sensitive fashion (Tilley et al. 2014). Here we synthesize a related probe specifically for the task of measuring conformational changes of endogenous ion channel voltage sensors. Importantly, we develop a method, grounded in statistical thermodynamics, to deconvolve conformational changes from images of probe fluorescence. We test the capabilities of the probe and deconvolution method by measuring protein conformational changes of endogenous ion channel voltage sensors in brain slices.

The probe described here reports conformational change of the voltage sensors of Kv2 proteins, which form voltage-gated K^+ channels. Like other members of the voltage-gated cation channel superfamily, Kv2 channels contain specialized 'voltage sensor domains' comprised of a bundle of four 'S1-S4' transmembrane helices (Long, Campbell, and Mackinnon 2005). The S4 helix contains positively charged arginine or lysine residues, 'gating charges', which harvest energy from voltage changes by moving through the transmembrane electric field (Aggarwal and MacKinnon 1996)(Islas and Sigworth 2001)(Islas and Sigworth 1999)(Seoh et al. 1996)(Tao et al. 2010) . When voltage sensor domains encounter a transmembrane voltage that is more negative on the inside of the cell membrane, voltage sensors are biased towards 'resting' conformations where gating charges are localized intracellularly. When voltage becomes more positive, gating charges translate towards the extracellular side of the membrane, and voltage sensors are progressively biased towards 'active' conformations, in a process of 'voltage activation'(Zagotta et al. 1994)(Zagotta, Hoshi, and Aldrich 1994).

The coupling of voltage activation to ion channels pore opening and downstream physiological processes has been extensively studied (Zheng and Trudeau, 2016). Activation of voltage sensor domains is coupled to the opening of pore domains within the ion channel, allowing conduction of ionic currents. The conformational change of ion channel voltage sensors can also have nonconducting functions by inducing conformational changes in nearby proteins. For example, in skeletal muscle, voltage activation of certain plasma membrane Ca^{2+} channels drives conformational changes in intracellular ryanodine receptor proteins (Rios and Brum 1987)(Schneider and Chandler 1973)(Tanabe et al. 1988).

Conformational changes of voltage sensors have been detected with electrophysiological measurements of gating currents (Armstrong and Bezanilla 1973)(Schneider and Chandler 1973)(Bezanilla 2018) or by optical measurements from fluorophores covalently attached to voltage sensors by genetic (Siegel and Isacoff 1997) or chemical engineering (Mannuzzu, Moronne, and Isacoff 1996). Each of these techniques have enabled breakthroughs in our understanding of how protein conformational changes are coupled to one another (Zheng and Trudeau, 2016). However, these existing techniques have limited utility for measuring voltage activation under physiological conditions: gating currents can only be measured when the proteins are expressed at high density in a voltage-clamped membrane; engineering fluorophores into voltage sensors irreversibly alters the structure and function of the labeled proteins. Here, we develop a different strategy, where fluorescent probes dynamically label voltage sensors to reveal conformational states.

Our probe reports voltage sensor activation of Kv2-type voltage-gated K^+ channels. Kv2 proteins form delayed-rectifier K^+ channels and contribute to many physiological outputs (Palacio et al. 2017)(Blaine and Ribera 2001)(Speca et al. 2014)(Du et al. 2000). The coupling between Kv2 voltage sensors and K^+ conduction is cell type specific and dynamically regulated (O'Connell, Loftus, and Tamkun 2010). Kv2 proteins also have nonconducting functions, including regulating exocytosis and plasma membrane–endoplasmic reticulum junctions (Fu et al. 2017)(Kirmiz, Palacio, et al. 2018)(Fox et al. 2015)(Fu et al. 2017)(Feinshreiber et al. 2010). Interest in understanding the dynamic coupling of Kv2 voltage sensors to their conducting and nonconducting physiological outputs has motivated the development of this probe.

Our Kv2 probe reports where voltage sensor conformational change occurs by selectively labeling resting voltage sensors. This conformation-selectivity comes from the peptide portion of the probe, a synthetic derivative of the tarantula peptide guangxitoxin-1E (GxTX). GxTX is a selective inhibitor of currents from Kv2 channels (Liu and Bean 2014)(Herrington et al. 2006)(Schmalhofer et al. 2009). GxTX has a high affinity for a resting voltage sensor conformation: 13 nM K_d for rat Kv2.1 in CHO-K1 cells (Tilley et al. 2014) . In this conformation, all gating charge is detained intracellularly. When the voltage sensor adopts active conformations, GxTX affinity becomes at least 5400-fold weaker (Tilley et al. 2018). When Kv2 voltage sensors are resting, fluorescently-tagged derivatives of GxTX label Kv2 proteins on the cell surface. When voltage sensors adopt active conformations, GxTX dissociates from the Kv2 proteins and diffuses away into the extracellular solution (Tilley et al. 2014). Thus, the intensity of fluorescent labeling of a cell's surface decreases as the degree of Kv2 voltage sensor activation increases.

Our goal is to exploit the conformation-selective binding of a GxTX-based probe to measure where and when in tissue Kv2 proteins adopt resting conformations. To do this we synthesized a probe compatible with two-photon imaging through light scattering tissue, and determined whether any fluorescence from tissue originates from probes bound to Kv2 channels. Crucially, we also develop a deconvolution method to extract measures of Kv2 voltage sensor conformational change from images of the conformation-selective probe. We then deploy the GxTX-based probe for two-photon imaging in brain slices, and find voltage-sensitive fluorescence changes consistent with originating from conformational changes of endogenous Kv2 neuronal channels.

Results

Throughout this study, we tested a probe developed from the tarantula peptide guangxitoxin-1E (GxTX) that is compatible with two-photon imaging. We have termed this probe, and others like it, Endogenous Channel Activity Probes or ECAPs. To generate this ECAP, we replaced the fluorophore on a previously presented ECAP that reports voltage-activation dynamics of a voltage gated ion channel with fluorescence change (Tilley et al. 2014). The prior ECAP is a synthetic derivative of the tarantula peptide guangxitoxin-1E (GxTX) conjugated to a DyLight 550 fluorophore (GxTX-550). However, DyLight 550 has poor two-photon excitation properties, so it was replaced with a dye that has more desirable photophysical properties. Alexa 594 exhibits a large two-photon excitation cross-section and ample spectral separation from green fluorescent protein (GFP), making it well-suited for multiplexed, two-photon experiments (Bestvater et al. 2002). We chemoselectively conjugated an Alexa 594-maleimide to a synthetic GxTX Ser13Cys derivative to create the ECAP used throughout this study, GxTX-594 (Fig 1 Supplement 1).

GxTX-594 colocalizes with Kv2.1 and Kv2.2, but not other K^+ channels

To determine whether this ECAP could potentially report activation of Kv2 channels in tissue, we first characterized its selectivity for Kv2 channels over other channels, each heterologously expressed in isolation. Previously, we had found that GxTX-550 labels Kv2.1 channels, but the selectivity of fluorescently-labeled GxTX derivatives for K^+ channel subtypes had not been determined (Tilley et al. 2014). To test the extent of GxTX-594 labeling of different K^+ channel types, we conducted multiplex imaging of GxTX-594 with GFP-tagged K^+ channel subunits in a CHO-K1 cell line, which do not express endogenous Kv channels. We first assessed whether GxTX-594 binds Kv2 channels. Mammals have two Kv2 pore-forming subunits, Kv2.1 and Kv2.2, both of which are expressed in neurons throughout the brain. CHO cells were transfected with either a rat Kv2.1-GFP or Kv2.2-GFP construct and were imaged 2 days later. Both Kv2.1-GFP and Kv2.2-GFP transfections yielded delayed rectifier K^+ currents (Fig 2, Supplement 1 A). Kv2.1-GFP and Kv2.2-GFP localized predominantly in clusters on the glass-adhered basal surface of CHO cells (Fig 1 A). Clustered basal expression is a hallmark of Kv2 channel localization in neurons and other mammalian cells when they are adhered to surfaces. In cultured HEK293 cells, COS-1 cells, and central neurons, these clusters mark cortical endoplasmic reticulum junctions with the plasma membrane (Cobb et al. 2015)(Kirmiz, Palacio, et al. 2018)(Kirmiz, Vierra, et al. 2018)(Fox et al. 2015)(Johnson et al. 2018)(Antonucci et al. 2001)(Johnson et al. 2018). GxTX-594 fluorescence localized to regions with GFP signal after

Kv2 transfected cells were incubated with 100 nM GxTX-594 for five minutes, indicating GxTX-594 labels surface Kv2.1 and Kv2.2 (Fig 1 A). Pearson correlation coefficients were calculated to quantify the colocalization between Kv2-GFP and GxTX-594 signals. Kv2.1-GFP and Kv2.2-GFP colocalized to GxTX-594 with an average Pearson correlation coefficient of 0.86 and 0.80, respectively, verifying a high degree of colocalization of both Kv2 proteins with GxTX-594 (Fig 1 B). The ratio of GxTX-594 to GFP fluorescence intensity was similar for Kv2.1 or Kv2.2 (Fig 1 B).

To test whether GxTX-594 binds other subtypes of K^+ channels, we tested whether its fluorescence would label other GFP-labeled K^+ channel subtypes. Electrophysiological assays with the native GxTX peptide concluded that it is more selective for Kv2 channels than any other known modulator, with only Kv4 channels showing any indication of modulation (Herrington 2007). However, electrophysiological testing only indicates whether GxTX modulates channels; electrophysiology would be unable to detect if GxTX benignly bound other channels, in a manner similar to antibodies which bind, but do not alter the currents of channels (Sack et al. 2013). Furthermore, the substitution of serine to cysteine at position 13 and the addition of Alexa 594 dye could potentially alter selectivity among channel subtypes. GFP-channel fusions were selected that had been demonstrated to express and retain function with a GFP tag: rat Kv4.2-GFP(Shibata et al. 2003), rat Kv1.5-GFP(Li et al. 2001), and mouse BK-GFP. Transfection of each of these channel subtypes into CHO cells resulted in voltage dependent outward currents, consistent with cell surface expression of functional channels (Fig 2, Supplement 1A). As not all channels localize to the basal membrane, GxTX-594 and channel-GFP imaging was conducted at a plane slightly above the basal surface for consistency. A wheat germ agglutinin (WGA) stain was used to identify the membrane surface. After incubation with 100 nM GxTX-594 for five minutes, Kv4.2, Kv1.5, and BK channels had little to no GxTX-594 fluorescence while Kv2.1 and Kv2.2 channels were clearly labeled (Fig 2, Supplement 1 B). When the background-subtracted GxTX-594:GFP fluorescence intensity ratio was normalized to Kv2.1, this ratio was close to zero for Kv4.2, Kv1.5, or BK (Fig 2, Supplement 1 C), suggesting minimal binding to these channel subtypes. Furthermore, no colocalization was apparent between Kv4.2, Kv1.5, or BK and GxTX-594 (Fig 2 Supplement 1 D). In these experiments we observed that the majority of GFP signal from Kv4.2 and Kv1.5 channels did not appear to colocalize with the WGA surface marker, suggesting the majority of channels were retained intracellularly (Fig 2, Supplement 1 B). More efficient cell surface expression was achieved by co-transfection with auxiliary subunits: Kv4.2 with KChIP2 (Shibata et al. 2003) and Kv1.5 with

Kvβ-2 (Shi et al. 1996). The experiments were repeated, with airydisk imaging for improved resolution (Fig 2 A). GxTX-594 fluorescence and colocalization was not apparent on cells expressing Kv4.2 + KChIP2, Kv1.5 + Kvβ-2, or BK (Fig 2 B and C). While not a complete survey of all the 80 voltage-gated ion channels in the mammalian genome, these results indicate that GxTX-594 fluorescence labels the location of Kv2 channels and not a subset of other K^+ channels with voltage sensors.

GxTX-594 binds Kv2.1 in the presence of its neuronal auxiliary subunit AMIGO-1

AMIGO-1 is an auxiliary subunit for Kv2 channels, that is colocalized with most if not all Kv2 channels in the brain (Peltola et al. 2011)(Bishop et al. 2018). AMIGO-1 is a single pass transmembrane protein with a large extracellular domain, an architecture similar to other auxiliary subunits that modulate binding of peptide toxins to other ion channels (Gilchrist et al. 2013)(Maffie et al. 2013)(Yu et al. 2016). To determine if AMIGO-1 affects GxTX-594 channel labeling, Kv2.1-expressing cells were transiently transfected with an AMIGO-1-YFP construct, and assayed for GxTX-594 binding. We used a CHO-K1 cell line stably transfected with rat Kv2.1 under control of a tetracycline-inducible promoter (Kv2.1-CHO)(Trapani and Korn 2003). Consistent with Kv2.1:AMIGO-1 colocalization observed in other cell types (Peltola et al. 2011)(Bishop et al. 2018). AMIGO-1-YFP fluorescence was observed in clusters at the basal membrane (Fig 3 A) similar to Kv2.1-GFP (Fig 1 A). GxTX-594 labeled both AMIGO-1 positive and AMIGO-1 negative cells (Fig 3 A). High Pearson's correlation coefficients indicated colocalization between AMIGO-1 and GxTX-594, consistent with AMIGO-1 colocalizing with clustered Kv2.1 (Fig 3 B). Increasing concentrations of GxTX-594 were applied to the cells and the relationship between GxTX-594 fluorescence intensity and dose was quantified for AMIGO-1 positive and negative cells (Fig 3 C). The Langmuir binding isotherm was fit to GxTX-594 fluorescence intensity (lines, Fig 3 D), and resulted in indistinguishable dissociation constants (K_d) between AMIGO-1 positive (27 nM ± 14) and AMIGO-1 negative cells (26.9 nM ± 8.3). While we do not know the stoichiometry of expression of AMIGO vs. Kv2.1 in these cells, there was no indication that AMIGO colocalization disrupted the GxTX-594–Kv2 interaction.

GxTX-594 fluorescence dynamics report Kv2 channel voltage activation

To image activity of ion channels, ECAP fluorescence needs to respond to changes in ion channel activity. To make conclusions about channel gating from ECAP fluorescence, the relation between ECAP fluorescence and channel conformational changes must be established. To assess whether GxTX-594 has a fluorescence response suitable for an ECAP, we measured how fluorescence intensity on cells expressing Kv2.1 responded to changes in voltage, subcellular localization, and temperature.

To assess the voltage response of GxTX-594 in a preparation with consistent levels of channel expression, we voltage clamped Kv2.1-CHO cells that had been cultured with minocycline for two days before imaging to induce Kv2.1 channel expression. For these experiments, Kv2.1-CHO cells were incubated in a bath solution containing 100 nM GxTX-594 for five minutes before dilution to 9 nM. This labeling protocol resulted in cell surface fluorescence emissions consistent with Alexa 594. Establishing the whole-cell voltage clamp configuration required at least 5 minutes after dilution to 9 nM, during which labeling was predicted to equilibrate (discussed below). Fluorescence intensity images were generated with airydisk confocal imaging. Cells were held at -80 mV and stepped to test potentials while measuring fluorescence (Fig 4 A). A region of interest (ROI) corresponding to the cell surface was manually identified and average fluorescence intensity quantified during time lapse sequences. Average fluorescence intensity from the cell surface was corrected by subtracting the average fluorescence intensity from an ROI in a region without cells to account for fluorescence from GxTX-594 freely diffusing in solution. Both the amplitude and kinetics of fluorescence change from cell surface ROIs appeared sensitive to voltage (Fig 4 B), similar to prior findings with GxTX-550 (Tilley et al. 2014). This suggests the mechanism underlying the voltage dependent fluorescence change of GxTX-594 is similar to GxTX-550: a conformational change in the voltage sensor of Kv2.1 causes a change in affinity for GxTX-594. Resultant binding or unbinding causes GxTX-594 to enter or leave imaging voxels containing Kv2.1 voltage sensors, and this movement of GxTX-594 is responsible for the apparent fluorescent labeling or unlabeling of the cell surfaces. Additionally, cells appeared to approach a baseline fluorescence intensity that was well above background fluorescence even when given a +80 mV depolarizing voltage stimulus (Fig 4 B). This residual fluorescence varied from cell to cell (Fig 4 C) potentially due to internalized GxTX-594 and auto fluorescence. However, some residual fluorescence appeared to be localized to the cell membrane (Fig 4 A) indicating that a population of GxTX-594 present in the membrane is insensitive to changes in voltage.

To determine which region of cells to quantitate fluorescence from, we compared the voltage dependent labeling at the center of the glass-adhered basal surfaces to the periphery. The confocal imaging plane containing the most GxTX-594 fluorescence was the basal surface (Fig 4 Supplement 1 A). In response to voltage change, the kinetics of fluorescence change were slower at center of the basal surface and faster towards the outer periphery (Fig 4 Supplement 1 B). We quantified rates of fluorescence change ($k_{\Delta F}$) by fitting a single exponential function (Equation 1), and found a progressive increase in $k_{\Delta F}$ as the ROI moved away from the center of cell (Fig 4 Supplement 1 C and D).

$$F = F_o + Ae^{\frac{(t-t_o)}{\tau}} \qquad \text{(Equation 1)}$$

This suggests the concentration of freely diffusing GxTX-594 in the restricted space between the cell membrane and the glass surface is transiently non-uniform after voltage change. The location dependence of $k_{\Delta F}$ was more pronounced during GxTX-594 labeling at -80 mV than unlabeling at +40 mV. We suspect that the more extreme location dependence at -80 mV is due to a high density of Kv2.1 binding sites in the restricted extracellular space between the cell membrane and coverslip, such that GxTX-594 is depleted from solution by binding Kv2.1 before reaching the center of the cell. After unbinding at +40 mV, each GxTX-594 molecule is less likely to rebind to Kv2.1 as it diffuses out from under the cell, because Kv2.1 voltage sensors are in an active, low affinity conformation (Tilley et al. 2014)(Tilley et al. 2018). This expected difference in GxTX-594 buffering by Kv2.1 could explain the difference in location dependence of $k_{\Delta F}$ during labeling and unlabeling. To avoid complications resulting from the variability of kinetics at the basal surface, voltage dependent labeling experiments were conducted while imaging at plane above the basal surface.

We next determined the range of voltages that triggered dynamic labeling of Kv2.1 by GxTX-594. We quantified labeling intensity by normalizing to initial fluorescence at a holding potential of -80 mV, and subtracting residual fluorescence after a +80 mV step to maximally unlabel channels ($F/F_{\text{init norm}}$). Steps to -40 mV reduced labeling to 70% $F/F_{\text{init norm}}$, and labeling decreased with increasing voltage such that steps to +40mV reduced labeling to 10% $F/F_{\text{init norm}}$ (Fig 4 C). The fluorescence–voltage response was fit with a Boltzmann function with a half maximal voltage midpoint ($V_{1/2}$) of -27 mV and a steepness (z) of 1.4 e_0 (Fig 4 C, black line). This is strikingly similar to the voltage dependence of integrated gating charge of Kv2.1 in the same cell line, without any GxTX present, $V_{1/2}$ = -26 mV, z = 1.6 e_0 (Tilley et al. 2018). This suggests that the degree of GxTX-594 labeling corresponds to the fraction of the channels' voltage sensors that have their gating charges in their most intracellular resting conformation. Although GxTX-based probes perturb the gating of the Kv2.1 channels they label (Tilley et al. 2014),these changes in fluorescence intensity appear to report conformational changes of the unlabeled channels.

To determine the temporal response to voltage change, we compared rates of GxTX-594 labeling and unlabeling (Fig 4 D). In response to voltage steps from a holding potential of -80 mV to more positive potentials, $k_{\Delta F}$ increased progressively as the voltage was increased above -40 mV, possibly beginning to saturate at positive voltages. These temporal response characteristics are similar to the GxTX-550 probe (Tilley et al. 2014). The $k_{\Delta F}$–voltage response was fit with a Boltzmann function with $V_{1/2}$ = +2 mV and z = 1.1 e_0 (Fig 4 D, black line). The relation of GxTX-594 labeling and unlabeling rate to conformational changes in Kv2.1 voltage sensors appears more complicated than the simple correspondence of fluorescence change the fraction of voltage sensor at rest. Notably, the dynamic fluorescence responses of GxTX-594 to voltage changes occurred at physiologically relevant potentials, suggesting that changes in GxTX-594 labeling intensity or rate could occur in response to changes in cellular electrical signaling.

We noted substantial variability between cells in the $k_{\Delta F}$ responses. We wondered if this could be due to fluctuations in ambient temperature (27-29°C), given the substantial temperature sensitivity reported for Kv2.1 conductance (F. Yang and Zheng 2014). To assess the temperature dependence of GxTX-594 labeling, the cell bath solution was heated to either 27°C or 37°C and stepped to 0 mV for a measurement of $k_{\Delta F}$ (Fig 4 Supplement 2). The fold change in $k_{\Delta F}$ over this 10 °C difference, or Q_{10}, was 3.8-fold. This was less than the up to 6-fold cell-to-cell variability observed under otherwise identical conditions. This indicates that the variation in $k_{\Delta F}$ is likely not attributed to temperature variation, and suggests it results from variability intrinsic to cells.

The probability of activation of unlabeled voltage sensors can be calculated from fluorescence dynamics

We developed a model relating ECAP labeling to voltage sensor activation. The ratio of labeled to unlabeled Kv2 is determined by binding and unbinding rates of the ECAP (Scheme A). These rates approach equilibrium when the membrane voltage remains constant producing a defined population of labeled and unlabeled channels. Labeling is voltage dependent because the binding and unbinding rates are different for resting and active conformations of voltage sensors. As voltage sensors change from a resting to an active conformation the binding rate of an ECAP decreases and the unbinding rate increases (Fig 4 E). The mechanism underlying the voltage dependence of binding is the increased affinity of an ECAP for resting vs active voltage sensor conformations. An increase in voltage establishes a new equilibrium for ECAP binding and a smaller population of channels are labeled. In order to capture these changes in binding and unbinding rates that drive the voltage dependence of ECAP dynamics, a more complex four-state model (Scheme B) is minimally required.

The scheme B model assumes the innate voltage sensitivity of the Kv2 channel is solely responsible for controlling voltage dependence.

Scheme B assumes that voltage sensor conformational changes equilibrate much faster than ECAP binding or unbinding, such that binding and unbinding are the rate limiting steps. As ECAP binding/unbinding occurs about 3 orders of magnitude more slowly than Kv2 channel gating, seconds and milliseconds respectively, the simplifying approximation that voltage sensor conformations are in constant equilibrium seems reasonable. We assume that the voltage sensor equilibria of Kv2 channels at any given voltage is described by a Boltzmann distribution (Equation 2):

$$K_{eq,Free} = e^{(V-V_{half,Unbound})} \cdot z \cdot (\frac{F}{RT}) \quad K_{eq,Bound} = e^{(V-V_{half,Bound})} \cdot z \cdot (\frac{F}{RT}) \quad \text{(Equation 2)}$$

Where $V_{1/2}$ is the voltage where the equilibrium constant = 1, z is the number of elementary charges determining voltage dependence, F is the Faraday constant, R is the ideal gas constant, and T is absolute temperature. In a separate study (Tilley et al. 2018) we measured Kv2.1 gating currents, and found that GxTX shifts all voltage sensor charge movement 73 mV more positive. The values of $V_{1/2}$ (41.3 mV) and z (1.5) from this dataset were input into Equation 2 in the model.

To relate voltage sensor activation to labeling and unlabeling, we determined binding rates (k_{on}[ECAP]) and unbinding (k_{off}) rates separately for resting and active voltage sensors. The microscopic rates for resting voltage sensors, $k_{on,Resting}$ and $k_{off,Resting}$ were determined from kinetic and equilibrium measures. In 10 nM GxTX-594, the rate $k_{\Delta F}$ appeared to stabilize below -40 mV where the fitted Boltzmann function approaches a rate of 7.6e-3 s-1 (Fig 4 D). We assume

$$k_{\Delta F} = k_{on}[ECAP] + k_{off} \qquad \text{(Equation 3)}$$

for resting voltage sensors. Using a K_d of 27 nM from GxTX-594 labeling of unpatched CHO cells (Fig 3 D), we assume

$$K_d = \frac{k_{off}}{k_{on}} \qquad \text{(Equation 4)}$$

to arrive at the $k_{on,Resting}$ and $k_{off,Resting}$ reported in Table 1. The estimate for $k_{off,Active}$ was obtained from the value of $k_{\Delta F}$ at extreme positive voltages, where the fitted Boltzmann function (Fig 4 D) approaches a rate of 0.31 s^{-1}. In 9 nM GxTX-594 at ≥40 mV, surface labeling become undiscernible from back ground, indicating the labeling rate is much smaller than the unlabeling rate and hence $k\Delta F \approx k_{off,Active.}$ While the particularly slow labeling of active voltage sensors made it difficult to measure $k_{on,Active}$ directly, the statistical thermodynamic principle of microscopic reversibility(Lewis 1925) constrained $k_{on,Active}$. We formalize this constraint here with an allosteric factor, C (Equation 5):

$$C = \frac{K_{eq,Bound}}{K_{eq,Unbound}} = \frac{K_{eq,Rest}}{K_{eq,Active}} = \frac{\frac{k_{off,Rest}}{k_{on,Rest}[Tx]}}{\frac{k_{off,Active}}{k_{on,Active}[Tx]}} \qquad \text{(Equation 5)}$$

At any static voltage, scheme B collapses into scheme A, where $k_{on,\ Total}$ is a weighted sum of both $k_{on,Resting}$ and $k_{on,Active}$ scheme B, and $k_{off,\ Total}$ is a weighted sum of $k_{off,Resting}$ and $k_{off,Active}$. The weights for $k_{on,Total}$ are the relative probabilities that unbound voltage sensors are resting or active, which is determined by the Boltzmann distribution at a specified voltage ($K_{eq,Unbound}$) (Equation 6):

$$k_{on,Total} = k_{on,Rest}[Tx] \cdot \frac{1}{1+K_{eq,Unbound}} + k_{on,Active}[Tx] \cdot \frac{1}{1+\frac{1}{K_{eq,Unbound}}} \qquad \text{(Equation 6)}$$

The total k_{off} is determined by the unbinding rate from resting voltage sensors ($k_{off,Rest}$) and the unbinding rate from active voltage sensors ($k_{off,Active}$). Similarly, these rates are adjusted by the relative probability that ECAP-bound voltage sensors are resting or active (Equation 7):

$$k_{off,Total} = k_{off,Rest} \cdot \frac{1}{1+K_{eq,Bound}} + k_{off,Active} \cdot \frac{1}{1+\frac{1}{K_{eq,Bound}}} \qquad \text{(Equation 7)}$$

Using $k_{on,Total}$ and $k_{off,Total}$ we can compute $k_{\Delta F}$ using Equation 3. To test the predictive value of the scheme A model, we compared the predicted $k_{\Delta F}$ to experimental measurements in 10 nM GxTX-594 (Fig 4 D). We conclude that the Scheme B model reasonably reproduced the voltage dependence of Kv2.1 labeling.

This simple 2-state model (Scheme A) also predicted the magnitude of the change in fluorescence with voltage. The fluorescence at any voltage (F) relative to fluorescence at an initial voltage ($F_{initial}$) is the ratio of the probabilities that the ECAP is bound at both voltages (Equation 8).

$$\frac{F}{F_{initial}} = \frac{P_{Bound,final}}{P_{Bound,initial}} \qquad \text{(Equation 8)}$$

The P_{bound} at any voltage can be determined from Scheme A where:

$$P_{Bound} = \frac{1}{1+K_{eq,Total}} = \frac{1}{1+\frac{k_{off,Total}}{k_{on,Total}\cdot[Tx]}} \qquad \text{(Equation 9)}$$

Using our model, we calculated the fluorescence–voltage relation from P_{bound} (Equation 8) and compared these calculated values to our experimental data. The model predicts fluorescence response within the range of the experimental data (Fig 4 C).

ECAP labeling reports average degree of activation of unlabeled voltage sensors

The Scheme A model relating labeling to voltage sensor activation was developed for static voltages. However, in electrically active cells, voltage is dynamic. For example, neurons fire action potentials during their electrical signaling. Action potentials occur on the millisecond time scale, orders of magnitude faster than the GxTX-594 response. Thus, the slow ECAP response will integrate voltage fluctuations occurring over many seconds. The scheme A model assumes that voltage sensors are at continuous equilibrium, and this assumption breaks down when voltage is rapidly changing. We determined whether our model could predict labeling during dynamic voltage changes.

To assess the response of GxTX-594 to a dynamic waveform, we stimulated voltage-clamped Kv2.1 cells with brief voltage steps that crudely mimic action potentials. We used simple 2 ms voltage steps from -80 to +40 mV. When repeated at 200 Hz, labeling decreased (Fig 5 A, B). To assess frequency response, step frequency was varied from 0.02 to 200 Hz. At frequencies higher than 25 Hz, detectable unlabeling occurred (Fig 11 C). Similar to the voltage dependence of this ECAP, $k_{\Delta F}$ varied with stimulus frequency as well (Fig 5 D).

Frequency-dependent predictions of F/F_{max} and $k_{\Delta F}$ were made from the Scheme A model. These predictions were calculated assuming the summed probability of being at each voltage (-80 or +40 mV) determines the overall P_{bound} (Equations 10 and 11).

$$k_{\Delta FHz} = (P_{40mV} \cdot k_{\Delta F40mV}) + (P_{-80mV} \cdot k_{\Delta F-80mV}) \qquad \text{Equation 10}$$

$$\mathrm{F}/F_{max} = (P_{40mV} \cdot \Delta F_{40mV}) + (P_{-80mV} \cdot \Delta F_{-80mV}) \qquad \text{Equation 11}$$

When predictions are compared to empirical measurements (blue lines, Fig 5 C and D), the predictions are within range of the measurements for frequencies less than 150 Hz. Generally, the model captures the waveform of the frequency dependence but predicts a weaker response than observed. In other words, the labeling changes occur at lower frequencies than they are predicted to, yet the slope of the predicted frequency dependence appears to be accurate. This discrepancy could be due to voltage sensor movement not being fully equilibrated by the end of the voltage steps. This is consistent with Kv2.1 gating currents which can have time constants of several milliseconds (Tilley et al. 2018). Despite the system not being in equilibrium at high frequencies, the predictions of the model were not far off, suggesting that the predictions of the model will be reasonably accurate at neuronal firing frequencies <150 Hz.

Labeling intensity is proportional to overall voltage sensor activation

We used the ECAP model (Scheme B, parameters from Table 1) to investigate general principles of the relation between voltage sensor activation and labeling. In particular, we were interested in using ECAP labeling to reveal information about voltage sensor activation in the unbound channel population. The model indicates that when an ECAP is applied at sub-saturating concentrations (below the K_d for resting voltage sensors), the change in labeling is proportional to the probability of unlabeled voltage sensors becoming active (Fig 6 A). This, perhaps counterintuitive, phenomenon emerges when the majority of voltage sensors are unlabeled, and this unlabeled majority dominates the response of the overall population. The lower the concentration of the ECAP, the better its labeling response predicts the voltage sensor activation of unlabeled channels. This model predicts that the degree of unlabeling with 10 nM GxTX-594 (Fig 4 C and 5 C), is nearly proportional to the degree of voltage sensor activation. Thus, a broadly qualitative conclusion can be made from ECAP fluorescence changes: a change in labeling occurs when the voltage sensors of unlabeled channels become more or less active.

Unlabeling kinetics are accelerated by voltage sensor activation

The ECAP model predicts the observed changes in voltage $k_{\Delta F}$ in 10 nM GxTX-594 (Fig 4 D). The voltage dependence of $k_{\Delta F}$ appears to saturate at extreme positive and negative voltages, and the model provides some insight into the thermodynamics underlying these responses. At extreme positive voltages, $k_{\Delta F}$ is almost exclusively determined by labeling and unlabeling of the active state. Similarly, at negative voltages, $k_{\Delta F}$ is determined by labeling and unlabeling of the resting state. Interestingly, as the concentration drops below the K_d of resting voltage sensors $k_{\Delta F}$ becomes insensitive to the concentration of ECAP (Fig 6 B) because the kinetics are determined primarily by k_{off} (Equation 3,7). Thus, all subsaturating concentrations of ECAPs are expected to produce similar $k_{\Delta F}$ responses. This result is useful as it indicates that if the concentration of ECAP is below the K_d, the fluorescence kinetics are expected to be consistent throughout a tissue as the ECAP diffuses through it, and insensitive to vagaries in concentration.

GxTX594 fluorescence response in brain slice appears consistent with activation of Kv2 channels

Having determined that GxTX-594 indicates the location of Kv2 channels, and developed a methodology to convert fluorescence changes into a measure of voltage sensor activation, we proceeded to assess its potential to report Kv2 activation in living tissue. We used scanning two-photon excitation to construct images of GxTX-594 fluorescence in cultured brain slices. In live tissue, we first determined whether GxTX-594 colocalized with overexpressed Kv2.1-GFP. Next, we assessed whether GxTX-594 fluorescence responded to depolarizing stimuli. Finally, we examined whether fluorescence from GxTX-594 labeled neurons could indicate the activity of endogenous Kv2 channels.

GxTX-594 colocalizes with Kv2 channels in brain slice

To test whether GxTX-594 can identify Kv2 channel location in neurons, we assessed its colocalization with Kv2.1-GFP. Brain slice cultures were sparsely transfected with Kv2.1-GFP, resulting in a small fraction of neurons displaying green fluorescence. When imaged two and four days after transfection, GFP fluorescence was seen evenly dispersed throughout the plasma membrane surrounding neuronal cell bodies and proximal dendrites (Fig 7 A, Fig 7 Supplement 1 A and B), suggesting that neurons may have had insufficient time to localize

Kv2.1-GFP to the endoplasmic reticulum–plasma membrane junctions where endogenous Kv2 channels have been found to reside (Kirmiz, Palacio, et al. 2018)(Kirmiz, Vierra, et al. 2018)(H I Bishop et al. 2015). Six days or more after transfection, Kv2.1-GFP fluorescence became more clustered on the cell soma and proximal processes, (Fig 7 B,C, Fig 7 Supplement 1 C green images) a pattern consistent with endogenous Kv2.1 (Fig 2 C , (Misonou et al. 2005)). After identifying a neuron expressing Kv2.1-GFP, perfusion was stopped and GxTX-594 was added to the static bath solution to a final concentration of 100 nM. After five minutes incubation, perfusion was restarted, leading to wash-out of GxTX-594 from the slice bath. After wash-out, GxTX-594 fluorescence colocalized with Kv2.1-GFP (Fig 7 A,B,C), indicating that GxTX-594 is able to diffuse through dense neural tissue and bind to neuronal Kv2 channels. We quantitated the degree of colocalization of GxTX-594 with Kv2.1-GFP using compressed stack images of the GFP transfected neurons. Pearson correlation coefficients confirmed the colocalization of GxTX-594 with Kv2.1-GFP in multiple slices (Fig 7 D). In most images of Kv2.1-GFP transfected neurons, similar punctate GxTX-594 labeling with was observed on neighboring untransfected neurons, suggesting that GxTX-594 also labeled endogenous Kv2 channels (Fig 7 C, white arrow).

In brain slice, punctate GxTX-594 fluorescence is modulated by neuronal depolarization, consistent with voltage activation endogenous of Kv2 channels

To test whether GxTX-594 labeling of brain slices is consistent with labeling of endogenous Kv2 voltage sensors, we determined whether GxTX-594 labeling responds to voltage changes. First, we looked for Kv2-like labeling patterns on CA1 pyramidal neurons in untransfected brain slices bathed in 100 nM GxTX-594. In two-photon optical sections thinner than the neuronal cell bodies, fluorescent puncta circumscribed dark intracellular spaces (Figure 8 A). This was similar to the pattern of fluorescence in Kv2.1-GFP expressing neurons (Figure 7 C), and consistent with the punctate expression pattern of Kv2.1 in CA1 pyramidal neurons seen in fixed brain slices (Misonou 2005). We tested whether the punctate fluorescence was voltage sensitive by voltage clamping neurons circumscribed by puncta. To ensure voltage clamp of the neuronal cell body, slices were bathed in tetrodotoxin to block Na^+ channels, and a Cs^+-containing patch pipette solution was used block K^+ channels. In each experiment a patch clamp pipette was lowered onto a GxTX-594 labeled neuron, and whole cell configuration was achieved with holding potential set to -70 mV. At this point time-lapse imaging of a two-photon optical section was initiated (Supplemental Movie 1). Depolarization to 0 mV resulted in loss of fluorescence from a subset of puncta surrounding the voltage-clamped neuron (Fig 8 B, red arrows). Other fluorescent puncta appeared unaltered by the 0 mV step (Fig 8 B, red arrows). To assess if the fluorescence decrease noted in some puncta after voltage step to 0 mV was due to random fluctuations during imaging, we compared fluorescence of the apparent cell membrane region to regions more distal from the patch-clamped cell body. To quantify this fluorescence change, an ROI 30 pixels (4.8 μm) wide containing the apparent membrane of the cell body was compared to other regions within each image (Fig 8 C). The region containing the membrane of the cell body lost fluorescence during the 0 mV step (Fig 8 D, ROI 1) while neither of the regions more distal (ROI 2&3), nor the intracellular region (ROI 0) showed a dramatic change. In multiple slices, the voltage-dependent decrease of fluorescence was similarly pronounced only in the region of the neuronal membrane (Fig 8 E). The kinetics of fluorescence response of the voltage-clamped membrane region was similar in multiple slices (Fig 8 F). Toe determine whether the fluorescence response to depolarization was driven by the Kv2-like puncta on the cell membrane, the fluorescence along a path containing the apparent cell membrane was selected by drawing a path connecting fluorescent puncta surrounding the dark cell body region, and averaging fluorescence within 5 pixels (0.8 μm) on either side of this path (Fig 8 G, yellow line). The fluorescence intensity along the path of the ROI revealed distinct peaks corresponding to puncta (Fig 8 H, red line). After stepping the neuron to 0 mV, the intensity of fluorescence of a subset of puncta lessened (Fig 8 H, black line, peaks 1,3,4,5,8). However, other puncta which appeared to be on the surface of the same cell body, maintained or increased in brightness (Fig 8 H, black line, peaks 2,6,7). These puncta could possibly represent Kv2 proteins on a neighboring cell, off-target or non-specific labeling by GxTX-594, or Kv2 channels that are unresponsive to voltage. When the kinetics of fluorescence intensity decay of individual voltage-sensitive puncta were fit with Eq. 1, $k_{\Delta F}$ values were within two-fold of each other (Fig 8 I), consistent with these spatially separated puncta all being on the surface of the voltage-clamped neuron.

To address whether the fluorescence change at the cell membrane was driven by decreases in regions of punctate fluorescence, the punctate and non-punctate fluorescence intensity changes were analyzed separately. The regions with fluorescence intensities above average for the path (Fig 8 H, dashed line) were binned as one group, and the regions with below average fluorescence binned as another. The above average group, by definition contained all punctate fluorescence. When comparing the fluorescence before and during the 0 mV step, the regions that were initially below average maintained the same intensity (103 ± 8%); regions of above average fluorescence decreased in the intensity (70 ± 8%). This suggests that the detectable unlabeling was driven by puncta.

The voltage response of this 100 nM GxTX-594 labeling in brain slice was similar to that predicted by the statistical thermodynamic model for Kv2.1 expressed in CHO cells (Fig 6 B, and Fig 8 K dotted line). To further determine how consistent the responses of brain slices and Kv2.1-expressing CHO cells were, we performed experiments with CHO cells under similar conditions as brain slice (100 nM GxTX-594, 30°C, Cs^+-containing patch pipette solution). $k_{\Delta F}$ values with 100 nM GxTX-594 on CHO cells were consistent with the predictions of the statistical thermodynamic model, and similar to brain slices (Fig 8 K).

We find that GxTX-594 labeling of neurons is consistent with GxTX-594 labeling endogenous Kv2 proteins. This conclusion is based on several metrics. The punctate GxTX-594 labeling of CA1 neurons is consistent with the patterns of endogenous Kv2 expression seen by immunofluorescence (Misonou et al. 2005)(H I Bishop et al. 2015)(Hannah I Bishop et al. 2018), and Kv2.1-GFP expression (Fig 7). GxTX-594 labels Kv2 proteins in the presence of its obligate neuronal auxiliary subunit AMIGO-1 (Fig 3), but does not label other related Kv proteins (Fig 2). The voltage response of GxTX-594 brain slice labeling was consistent with labeling of Kv2.1. Steps to 0 mV resulted in unlabeling by GxTX-594 in CHO cells (Fig 4) and neurons (Fig 8), and the kinetics of this unlabeling were similar (Fig 8 J). Altogether, these results are consistent with the GxTX-594 probe labeling endogenous Kv2 channels in rat CA1 hippocampal pyramidal neurons and unlabeling in response to activation of their voltage sensors.

Discussion

The results presented herein suggest that GxTX-594 acts as an endogenous voltage sensor probe. Specifically, we found that:

1) GxTX-594 is a two-photon imaging compatible molecular probe that selectively binds resting conformations of Kv2 voltage sensors.

2) Functions derived from statistic thermodynamics can deconvolve changes in Kv2 labeling into a measure of voltage sensor conformational change.

3) Voltage-dependent fluorescence changes in brain slices are consistent with fluorescence changes expected from endogenous Kv2 voltage sensors.

Together these results indicate that tracking the fluorescence of conformation-dependent ligands such as GxTX-594 can reveal conformational changes of endogenous proteins. Below we discuss physiological questions that could be addressed with a GxTX-based Kv2 voltage sensor probe, the limitations of GxTX-594 as a probe, and the potential for conformation-selective ligands to be engineered into imaging probes for your protein of interest.

A voltage sensor probe to study Kv2 physiology

The GxTX-594 probe revealed conformational changes of Kv2 voltage sensors. Activation of Kv2 voltage sensors is required for opening of its K^+-conductive pore (Islas and Sigworth 1999). Cells dynamically regulate the voltage sensitivity of Kv2 channel pore opening (MacDonald, Salapatek, and Wheeler 2003)(Mandikian et al. 2014)(Misonou et al. 2005)(Murakoshi et al. 1997)(Redman et al. 2007)(Misonou et al. 2006)(Plant et al. 2011). It is unknown whether these regulatory processes impact voltage sensor movement directly, or impact conformational changes that are coupled to voltage sensor movement, such as pore opening. By specifically measuring voltage sensor movements, the mechanisms by which pore opening is regulated can be better understood. In studies of the mechanism of cellular regulation of Kv2.1 in HEK cells, it was concluded that voltage sensor movements were decoupled from pore opening in the majority of channels with punctate localization (O'Connell, Loftus, and Tamkun 2010)(Fox, Loftus, and Tamkun 2013). This conclusion was supported by assessing movement of voltage sensors with gating currents, currents arising from the movement of voltage sensors themselves. Gating current measurements are feasible only in cell preparations where a sufficiently high density of voltage sensors can be voltage clamped. This density requirement has resulted in gating current measurement being most commonly conducted in heterologous expression systems, such as HEK cells. Measurements of endogenous gating currents have been restricted a limited number of cell preparations such as invertebrate giant axons and muscle cells. Gating currents or other measures of conformational change of endogenous voltage sensors have never, to our knowledge, been measured in a brain slice.

The GxTX-594 probe has revealed the first glimpse of how Kv2 voltage sensors are operating in a tissue. Our results indicate that the voltage sensors of endogenous Kv2 proteins clustered on the surface of CA1 pyramidal neurons in rat hippocampus are responsive to voltage. This is consistent with the proposal of Tamkun and colleagues, extrapolating from gating current measurements in HEK cells. Additionally, the kinetics of the GxTX-594 response to voltage were similar in brain slice and CHO cells, indicating that the stimulus-response relation between transmembrane voltage and voltage sensor conformational change is similar in the two situations.

Conformational change of the voltage sensors of ion channels can trigger cellular signaling processes besides opening the protein's ion conductive pore. For example, conformational change in the voltage sensors of calcium channels is coupled to conformational change of ryanodine receptors in the sarcoplasmic reticulum of skeletal muscle (Rios and Brum 1987). Kv2 channels have nonconducting functions: Kv2 channels recruit endoplasmic reticulum to the plasma membrane(Fox et al. 2015); Kv2.1 binds syntaxin proteins and influences exocytosis (Feinshreiber et al. 2010)(Greitzer-Antes et al. 2018)(Singer-Lahat, Chikvashvili, and Lotan 2008). Whether Kv2 voltage sensor conformational change influences these nonconducting functions is unknown. By reporting voltage sensor activation, the GxTX-594 probe could potentially be used to determine whether voltage sensor conformational change is crucial for the nonconducting functions of Kv2 proteins.

Limitations of using GxTX-594 to measure conformational change

The ability of conformation-selective probes to report conformational change is inherently limited. Some limitations result from the properties of the particular probe deployed, while other limitations are inherent to the mechanism of conformation-selective binding. We discuss limitations of GxTX-594 and how those limitations can be managed in the realms of temporal resolution, signal to noise, protein modulation by probes, and errors in interpretation of images.

Temporal resolution. With GxTX-594, the average probability that voltage sensors are activated (P_{act}), can be measured. GxTX-594 requires seconds to respond, much slower than the membrane voltage changes associated with action potentials. Probes with faster kinetics will allow measurements of faster patterns of channel activity. Modifying probe kinetics becomes a question of sensor design and toxin engineering; the response properties of probes can be readily altered by chemical modification of side chain residues, allowing the dynamics to be optimized in next-generation probes. Ultimately the response time of any conformation-selective probe will be limited by the labeling rate which is a product of the probe's concentration and its inherent association constant.

Signal to noise. The fluorescence signal intensity from GxTX-594 limited spatial and temporal resolution, estimates of P_{act}, and interpretation of data. Continuing advances in microscopy will undoubtedly improve fundamental signal to noise of fluorescence imaging in tissue. However, the signal to noise in all experiments is ultimately limited by the photophysics of the fluorophore as well as photodamage to the probe and tissue. Probes with improved fluorescence characteristics are expected to improve the ultimate signal to noise. Quantum dot nanoparticles offer orders of magnitude improvement in signal to noise for one- and two-photon excitation microscopy methods. We have developed synthetic methods for making Kv2 quantum dot ECAPs from GxTX (Mann et al. 2018). These probes are expected to respond to Kv2 channel voltage sensor activation with similarly interpretable fluorescence changes, yet offer orders of magnitude improvements in signal to noise ratio. A major contributor to signal to noise is fluorescence due to non-specific and off-target binding. The affinity and specificity of the GxTX peptide that guides the fluorophore to Kv2 will presumably influence non-selective fluorescence. Additionally, incubation with GxTX-594 eventually leads to intracellular accumulation of fluorescence in Kv2-expressing CHO cells, presumably due to internalization of Kv2–GxTX-594 complexes; we have not determined the extent to which this internalization occurs in brain slices.

Protein modulation by probes. GxTX-based probes inhibit the Kv2 channels they bind. Thus, they deplete the population of channels responding normally to physiological stimuli. This is a general problem with molecular probes: they disrupt the process they report (e.g. free calcium indicators deplete free calcium). This probe perturbation problem can be minimized by working with low concentrations of probe to inhibit a minimal subset of the total Kv2 population. Channel activity can be recorded optically even when only a small fraction of Kv2 channels are affected (Tilley et al. 2014). Furthermore, as indicated in Figure X, GxTX-594 most accurately reports conformational change when used at sub-saturating concentrations. Thus, low concentrations are optimal for both accuracy of measurement and minimizing the perturbation of physiology.

Errors in interpretation of images. The models enabling deconvolution of conformational change involve approximations. The statistical thermodynamics developed here involve ligand binding and conformational change dynamics using approximations of Eyring rate theory (Eyring 2004). Thus, models will always have limitations stemming from the necessary approximations. The model of Kv2 voltage sensor conformational change developed here is an oversimplification. While the gating dynamics of Kv2 channels have never been fully described with an explicit thermodynamic model, they are certainly more complex than our model. Our model assumes each of the of the channel's 4 voltage sensors bind 1 GxTX, and that the 4 voltage sensors change conformation independently of each other. However, Kv2 channels exhibit cooperative gating when they open their pores, and pore opening impacts voltage sensors (Tilley et al. 2018)(Islas and Sigworth 1999)(Scholle et al. 2004)(Jara-Oseguera et al. 2011). Under some conditions the assumption of voltage sensor independence may limit the models' predictive power. Additionally, the model of GxTX-594 labeling developed here assumes that voltage sensors are in continuous equilibrium. This simplification is expected to result in diminished accuracy during high frequency voltage changes, such as during action potentials. These deviations from equilibrium could explain the deviation of the model from the data in response to high frequency voltage steps (Fig 5D).

Conformation-selective probes reveal conformational change of endogenous proteins

If the limitations of conformation-selective binding are given proper consideration, deconvolution of fluorescence intensities can reveal conformational changes of endogenous proteins (Irannejad et al. 2013)(Koide et al. 2002). Importantly, measurements of dynamic labeling by a conformation-selective probe, such as GxTX, can enable deduction of how unlabeled proteins behave, despite the fact that GxTX nearly completely inhibits Kv2 voltage sensor movement of the subunit it binds, and only proteins that are bound by a fluorescent GxTX-based probe generate optical signals (Tilley et al. 2014)(Tilley et al. 2018). This approach is analogous to calcium imaging experiments, which have been spectacularly informative about physiological calcium signaling (W. Yang and Yuste 2017), despite the fact that no optical signals originate from the physiologically relevant free Ca^{2+}, only from Ca^{2+} that is chelated by a dye. In all such experiments, fluorescence from Ca^{2+}-bound dyes is deconvolved using the statistical thermodynamics of Ca^{2+} binding to calculate free Ca^{2+} (Adams 2010). Similarly, GxTX-based probes are dynamically binding to unlabeled Kv2 proteins, and the binding rate is dependent on the probability that unlabeled voltage sensors are in a resting conformation (Fig 6). Thus, the conformations of unlabeled Kv2 proteins influence the dynamics of labeling with GxTX-based probes. Consequently, the dynamics of labeling reveal the conformations of unlabeled Kv2 proteins.

Deployment of GxTX-594 to report conformational changes of endogenous channels demonstrates that conformation-selective ligands can be used to image occurrence of the conformations they bind to. The same principles of action apply to any conformation-selective labeling reagent, suggesting that probes for conformational changes of many different proteins could be developed. Probes could conceivably be developed from the many other voltage sensor toxins and other gating modifiers that act by a similar mechanism as GxTX, yet target the voltage sensors of different ion channel proteins (Peretz et al. 2010)(McCormack et al. 2013)(Ahuja et al. 2015)(Zhang et al. 2018)(Catterall et al. 2007)(Dockendorff et al. 2018)(Sack, Aldrich, and Gilly 2004).

Conformation-selective binders have been engineered for a variety of other proteins, yet methods to quantify conformational changes from their fluorescence are needed. For example, fluorescently-labeled conformation-selective binders have been used to understand GPCR signaling (Irannejad et al. 2013). These GPCR probes are GFP-tagged recombinant camelid antibodies that bind to GPCRs with enhanced affinity when the GPCRs adopt activated conformations. GPCR probes have revealed that endocytosed GPCRs continue to remain in a physiologically active conformation, leading to the proposition that substantial GPCR signaling takes place in endosomes (Tsvetanova, Irannejad, and von Zastrow 2015)(Eichel and von Zastrow 2018). However, a means to measure the conformational equilibria of GPCRs from probe fluorescence has not yet been developed. The statistical thermodynamic framework developed here could provide a starting point for more quantitative interpretation of time-lapse imaging of these GPCR probes.

Probes such as GxTX-594 that bind select conformations of ion channels are expected to have the general response properties displayed in Figure 6. That is, as the equilibrium between conformations changes, the probe will label or unlabel at different rates. Importantly, when concentrations of a probe are less than the apparent K_d, fluorescence change becomes proportional to conformational change of unlabeled proteins. We suggest that generation of further conformation-dependent probes and models to interpret their fluorescence could allow the measurement of conformational equilibria of a wide variety of endogenous proteins.

Figure Legends

Figure 1: **GxTX-594 colocalizes with Kv2-GFP channels.**

A. Fluorescence from CHO cells transfected with Kv2.1-GFP (Top Row) or Kv2.2-GFP (Bottom Row) and labeled with GxTX-594. Imaging plane was near the glass adhered cell surface. Cells were incubated with 100 nM GxTX-594 for 5 minutes and rinsed before imaging. Fluorescence shown corresponds to emission of GFP (Left), Alexa 594 (middle), or an overlay of GFP and Alexa 594 channels (right).

B. Pearson correlation coefficient for GxTX-594 colocalization with Kv2.1-GFP (N=1, n=8) or Kv2.2-GFP (N=1, n= 7) (Top). Ratio of Magenta to green intensity between GxTX-594 and Kv2-GFP (Bottom). Scale bar is 20 µm.

Figure 1Supplement1: **Synthesis of GxTX-594**

A. Molecular model for Alexa-594 conjugated to GxTX-Ser13-(Cys). Thiol-Maleimide conjugation chemistry was used to synthesize the fluorescent probe.

B. HPLC chromatogram and MALDI-TOF MS profile for GxTX-Ser13-Cys. GxTX-Ser13-Cys eluted at 12.6 minutes which corresponds to 33 % Acetonitrile.

C. HPLC profile for GxTX-594 post the conjugation reaction between Alexa-594 and GxTX-Ser13-(Cys). 1 is GxTX-Ser13-Cys (Retention time: 12.8 minutes, 33% Acetonitrile), 2 is the minor product from conjugation, and 3 is the major product from conjugation (Retention time: 16.4 minutes, 35% Acetonitrile) which was further purified and used for experiments.

D. HPLC and MALDI-TOF MS profile for GxTX-594. 2 is the minor product and 3 is the major product which was used in experimental assays. GxTX-594 (3) eluted at 12.5 which corresponds to 33 % ACN.

Figure 2: **GxTX-594 is selective for Kv2 channels.**

A. Fluorescence from live CHO cells transfected with Kv2.1-GFP, Kv2.2-GFP, Kv4.2-GFP + KChIP2, Kv1.5-GFP+Kvβ2, or BK-GFP (labeled by row) and labeled with GxTX-594. Imaging plane was at the solution exposed surface which is higher than the glass adhered surface. Cells were incubated with 100 nM GxTX-594 and 5 μg/mL WGA405 which binds to carbohydrates in the plasma membrane and rinsed before imaging. Fluorescence shown corresponds to emission of GFP (Column 1), Alexa 594 (Column 2), WGA405 (Column 3), or an overlay of GFP, Alexa 594, and WGA405 channels (Column 4)

B. Background subtracted GxTX-594:GFP ratio for different GFP and K^+ channel subtypes normalized to the average GxTX-594:Kv2.1-GFP ratio. The area of an image that contained no cells was selected as background.

C. Pearson correlation coefficients between GxTX-594 and GFP. Pearson values were calculated in imageJ. Colocalization for individual cells was determined using hand drawn ROIs around the cell membrane using the WGA405 fluorescence as a membrane proxy.

Kv2.1 n = 16, Kv2.2 n = 10, Kv4.2 n = 13, Kv1.5 =13, BK n =10. For all K+ subtypes N=1. N refers to the number of plates imaged for each transfected subtype and n refers to the number of cells analyzed in each plate. The same cells were used for analysis in B and C. Scale bars are 20 μm. Significant differences were observed between Pearson value and GxTX:GFP ratio for Kv2.1 or Kv2.2 and Kv1.5, 1.4, or BK by Mann-Whitney ($p<0.0001$)

Figure 2 Supplement 1: **GxTX-594 colocalizes with Kv2 ion channels**

A. Exemplar whole - cell voltage clamp recordings of CHO cells expressing Kv 2.1-GFP, Kv 2.2 GFP, Kv4.2-GFP, Kv1.5-GFP, or BK-GFP. Recordings shown are representative responses to 100 ms steps from - 100 mV to -40, 0 and +40 mV.

B. Fluorescence from live CHO cells transfected with Kv2.1-GFP, Kv2.2-GFP, Kv4.2-GFP Kv1.5-GFP, or BK-GFP (labeled by row) and labeled with GxTX-594. Imaging plane was at the solution exposed surface which is higher than the glass adhered surface. Cells were incubated with 100 nM GxTX-594 and 5 μg/mL WGA405 which binds to carbohydrates in the plasma membrane and rinsed before imaging. Fluorescence shown corresponds to emission of GFP (Column 1), Alexa 594 (Column 2), WGA405 (Column 3), or an overlay of GFP, Alexa 594, and WGA405 channels (Column 4)

C. Background subtracted GxTX-594:GFP ratio for different GFP and K^+ channel subtypes normalized to the average GxTX-594:Kv2.1-GFP ratio. The area of an image that contained no cells was selected as background.

D. Pearson correlation coefficients between GxTX-594 and GFP. Pearson values were calculated in imageJ. Colocalization for individual cells was determined using hand drawn ROIs around the cell membrane using the WGA405 fluorescence as a membrane proxy.

Kv2.1 n = 11, Kv2.2 n = 9, Kv4.2 n = 13, Kv1.5 = 13, and BK n =12. For all K+ subtypes N=2. N refers to the number of plates imaged for each transfected subtype and n refers to the number of cells analyzed in each plate. The same cells were used for analysis in C and D. Scale bars are 20 μm.

Figure 3: **GxTX594 binds Kv2.1 in the presence of its auxiliary subunit AMIGO-1.**

A. Fluorescence from Kv2.1-CHO cells transfected with AMIGO-1-YFP. Imaging plane was near the glass adhered cell surface. Cells were incubated in respective concentrations of GxTX-594 for 15 minutes. GxTX-594 images in each panel represents fluorescence after indicated concentration was washed out. Fluorescence shown corresponds to YFP (Green) and Alexa 594 (Magenta). Scale bar is 20 μm.

B. Pearson correlation coefficient between YFP and GxTX-594. Amigo positive ROIs were used as a mask when measuring colocalization between Amigo-1-YFP and GxTX-594. An exemplar ROI for AMIGO-1 positive cells is shown in A. n=8 N=3 (n is the number of cells analyzed N is the number of dose response experiments performed).

C. Fluorescence intensity during the dose response experiment shown in A. The grey trace represents AMIGO-1 positive (YFP positive) cells while the black trace represents AMIGO-1 negative (YFP negative) cells . AMIGO-1 positive cells were selected by hand drawing an ROI around cells that expressed AMIGO-YFP while AMIGO-1 negative cells were selected by drawing an ROI around cells that showed evident GxTX-594 labeling but no AMIGO-YFP expression. An exemplar of the ROI used for AMIGO-1 positive cells is shown in A. Traces were not background subtracted but were normalized to the max fluorescence that was reached during incubation with 1000 nM GxTX-594.

D. Changes in fluorescence were analyzed at each concentration from multiple dose response experiments. Different symbols correspond to different experiments (N=3). Global fits for the data were done using the Hill equation with the slope held at 1 to obtain a dissociation constant (K_d) for GxTX-594. The K_d from these fits are 26.7 nM ± 14.3 for AMIGO-1 positive cells and 26.9 nM ± 8.3 for AMIGO-1 negative cells.

Figure 4: **GxTX-594 labeling responds to transmembrane voltage.**

A. GxTx-594 fluorescence intensity on Kv2.1 expressing CHO cells incubated in 100 nM GxTX-594 for 5 minutes. GxTx-594 was diluted to 9 nM before starting voltage stimuli. Rows indicate voltage steps from a holding potential of -80 mV. Columns indicate time after voltage steps. Images were taken at the solutions exposed surface which is higher than the glass adhered surface. Scale bar is 10 µm.

B. Representative traces for GxTX-594 labelling decay at indicated voltages. Traces were fit with using Eq. 1. Fits are overlaid and are the same color as the corresponding trace. The rate of fluorescence change (kΔF) at each voltage were obtained from these fits. The kΔF measured for -40 mV, 0 mV, 40 mV and 80 mV were 2.2e-2 ± 2.2e-3 s^{-1}, 1.3e-1 ± 2.3e-3 s^{-1}, 2.6e-1 ± 6.2e-3 s^{-1}, and 5.3e-1 ± 1.1e-2 s^{-1} respectively. ROIs were hand drawn capturing the cell membrane based on GxTX-594 fluorescence. Background was determined by taking the average fluorescence of a region that did not contain cells over the time course of the voltage protocol. This average was subtracted from each experimental group. Traces were normalized to initial fluorescence intensity before the application of the voltage stimulus.

C. Change in fluorescence after maximal unlabeling (+80mV stimulus) for multiple CHO cells. Each point represents one CHO cell. Background subtraction and normalization methods are the same as described in B.

D. Decrease in fluorescence at increasing voltages for multiple cells (Different colors represents different cells) when stepped to indicated voltages from a holding potential of -80 mV for 50 s. Error bars are Standard Error of Mean from average fluorescence change at each voltage. Black line represents global fit when all the data were fit using the Boltzmann equation ($V_{1/2}$ = -27.39 ± 2.48, z= 1.38 ± 0.13, n held at 1, A held at -100). Blue line represents decreases in fluorescence at increasing voltages derived from the model shown in scheme B at a concentration of 10 nM. Note the close overlap between experimental and model generated data set. Traces were normalized to initial fluorescence intensity at -80 mV before the application of the voltage stimulus. Additionally, the plot was scaled by subtracting the residual fluorescence intensity after a +80 mV step.

E. GxTX-594 unlabeling rates (kΔF) at increasing voltages for multiple cells (Different colors represent different cells). Rates were obtained from fitting decreases in fluorescence with Eq. 1 as shown in B, except for the rates at -80 mV which were obtained by fitting increases in fluorescence after depolarization steps with Eq. 1. Error bars are the Standard Error of Mean from the average rate of fluorescence change at each voltage. Black line represents a global fit when all data were fit using the Boltzmann equation ($V_{1/2}$ =2.26 ± 7.89, z= 1.14 ± 0.38, n is held at 1, A is 1.61). Blue line represents the rates of fluorescence change at increasing voltages derived from the model shown in scheme B at a concentration of 10 nM.

Figure 4 Supplement 1: **GxTX-594 kinetics is impacted by restricted regions.**

A. GxTX-594 fluorescence from Kv2.1 channels in CHO cells. Image plane is near the glass-adhered surface. ROIs are indicated in yellow. Scale bar is 10 μm

B. Representative traces for GxTX-594 labelling decay at indicated voltages. Traces were fit using Eq. 1 for both unlabeling at 40mV and labeling at -80 mV. Fits are overlaid and are in red. The rate of fluorescence change (kΔF) at each ROI was obtained from these fits. The kΔF measured during the 40mV step for ROI 1, 2, 3 and 4 were 4.3e-2 ± 2.6e-3 s^{-1}, 4.4e-2± 1.6e-3 s^{-1}, 5.7e-2 ± 1.5e-3 s^{-1}, and 9.7e-2 ± 3.3e-3 s^{-1} respectively. The kΔF measured when cells were returned to -80mV for ROI 1, 2, 3 and 4 were 4.3e-4 ± 1.1e-5 s^{-1}, 7.9e-4 ± 5.3e-6 s^{-1}, 2.8e-3 ± 7.4e-6s^{-1}, and 5.5e-3 ± 1.3e-4 s^{-1} respectively. ROI 4 was hand drawn capturing the cell membrane based on GxTX-594 fluorescence. ROI 1,2, and 3 are concentric circles. Background was determined by taking the average fluorescence of a region that did not contain cells over the time course of the voltage protocol. This average was subtracted from each experimental group. Traces were normalized to initial fluorescence intensity before the application of the voltage stimulus.

C. The off rate at 40 mV for multiple cells when ROIs were drawn as depicted in A. Individual cells are represented by different colors.

D. The on rate at -80 mV for multiple cells when ROIs were drawn as depicted in Individual cells are represented by different colors.

Figure 4 Supplement 2: **Temperature dependence of GxTX-594 on Kv2.1 CHO cells.**

A. Representative traces for GxTX-594 labelling decay when depolarized to 0 mV from a holding potential of -80 mV at 27°C (black) and 37°C (gray). Traces were fit with using Eq. 1. Fits are overlaid and are the same color as the corresponding trace. The rate of fluorescence change (kΔF) at both temperatures were obtained from these fits. The kΔF measured for 27°C (black) and 37°C (gray) were 2.8e-2 ± 3.9e-3 s^{-1}, and 7.5e-2 ± 5.4e-3. Background was determined by taking the average fluorescence of a region that did not contain cells over the time course of the voltage protocol. This average was subtracted from each experimental group. Traces were normalized to initial fluorescence intensity before the application of the voltage stimulus.

B. Rate of fluorescence change in multiple cells at 27°C and 37°C. The rate of fluorescence change is significantly faster at higher temperatures (p=0.0005). A Q10 of 3.8 was calculated between 27°C and 37°C. Each point represents one cell n=7.

Figure 5: **GxTX-594 fluorescence has a frequency dependence**

A. GxTx-594 fluorescence intensity on Kv2.1 expressing CHO cells incubated in 100 nM GxTX-594 for 5 minutes. GxTx-594 was diluted to 9 nM before starting frequency stimuli. GxTX-594 fluorescence before frequency stimulus (Left), after 50s of 200 Hz stimulus (Middle), and 100 s after the cell is returned to resting potential of -80 mV (Right). Note that in each panel the unpatched cell (left cell) does not show a change in fluorescence. Scale bar is 10µm.

B. Representative trace for GxTX-594 unlabeling at 200 Hz. The trace was fit using Eq. 1. Fit is overlaid and is in red. The rate of fluorescence change k∆F) at 200 Hz was obtained from this fit. The k∆F measured for 200 Hz was 0.223 ± 9.96e-3 s^{-1}. ROIs were hand drawn capturing the cell membrane based on GxTX-594 fluorescence. Background was determined by taking the average fluorescence of a region that did not contain cells over the time course of the frequency protocol. This average was subtracted from each experimental group. Traces were normalized to initial fluorescence intensity before the application of the frequency stimulus.

C. Decrease in fluorescence at increasing frequency for multiple cells (Different colors represents different cells) when stepped to indicated frequencies from a holding potential of -80 mV. Error bars are Standard Error of Mean from average fluorescence change at each frequency. Black line represents global fit when all the data were fit using the Boltzmann equation ($V_{1/2}$ = -0.35 ± 0.035, z= 51.2 ± 4.2, n held at 1, A held at -1). Blue line represents decreases in fluorescence at increasing voltages derived from the model shown in scheme B at a concentration of 10 nM. Traces were normalized to initial fluorescence intensity at -80mV before the application of the frequency stimulus.

D. GxTX-594 unlabeling rates (k∆F) at increasing frequencies for multiple cells (Different colors represent different cells). Rates were obtained from fitting decreases in fluorescence with Eq. 1 as shown in B. Error bars are the Standard Error of Mean from the average rate of fluorescence change at each frequency. Black line represents a global fit when all data were fit using the Boltzmann equation ($V_{1/2}$ =-0.67 ± 0.007, z= 79.8 ± 1.9, n is held at 1, A is 1.29). Blue line represents the rates of fluorescence change at increasing frequencies derived from the model shown in scheme B at a concentration of 10 nM.

Figure 6: **Model of GxTX-594 binding relates fluorescence response to probability of channel activation.**

A. Model predicted changes in fluorescence at different voltages for indicated concentrations (Left). Relation between change in fluorescence and probability of activation at various concentrations (Right). Dotted black line represents the probability that unliganded voltage sensors are active at different voltages based on a 4th order Boltzmann distribution.

B. Model predicted rates for changes in fluorescence at different voltages for indicated concentrations (Left). Relation between rates of fluorescence change and probability of activation (Right).

Figure 7: **GxTX-594 labels CA1 hippocampal pyramidal neurons transfected with Kv2.1-GFP.**

A. Rat CA1 hippocampal pyramidal neuron four days after transfection with Kv2.1-GFP (Left), labeled with 100 nM GxTX-594 (Middle) and overlay (Right). Kv2.1 four days after transfection exhibits a dispersed expression pattern through the soma and dendrites
B. Rat CA1 hippocampal pyramidal neuron six days after transfection with Kv2.1-GFP (Left), labeled with 100 nM GxTX-594 (Middle) and overlay (Right). Kv2.1 six days after transfection exhibits a clustered expression pattern through the soma and dendrites
C. GxTX-594 labels both Kv2.1- GFP punctae and endogenous Kv2.1 channels in the same frame.
D. Pearson correlation coefficients from CA1 hippocampal neurons six days after transfection with Kv2.1-GFP shows a high degree of colocalization. Each point represents a different neuron (n=6). Colocalization analysis combines Kv2.1-GFP transfected neurons from both four days and six days post transfection

All scale bars are 10 μm.

Figure 7 Supplement 1: **GxTX-594 labels CA1 hippocampal pyramidal neurons transfected with Kv2.1-GFP.**

A. Rat CA1 hippocampal pyramidal neuron two days after transfection with Kv2.1-GFP (Left), labeled with 100 nM GxTX-594 (Middle) and overlay (Right).
B. Rat CA1 hippocampal pyramidal neuron four days after transfection with Kv2.1-GFP (Left), labeled with 100 nM GxTX-594 (Middle) and overlay (Right). Kv2.1 four days after transfection exhibits a dispersed expression pattern through the soma and dendrites
C. Rat CA1 hippocampal pyramidal neuron six days after transfection with Kv2.1-GFP (Left), labeled with 100 nM GxTX-594 (Middle) and overlay (Right). Kv2.1 six days after transfection exhibits a clustered expression pattern through the soma and dendrites

Figure 8: **GxTX-594 puncta on hippocampal CA1 neurons are sensitive to voltage stimulus**

A. 2-photon excitation image of fluorescence from CA1 pyramidal neurons in a cultured hippocampal slice after incubation with 100 nM GxTX-594. This projected image was reconstructed from a series of optical slices. Scale bar is 10 μm.

B. Response of GxTX-594 fluorescence to depolarization. A whole cell patch-clamped neuron was held at indicated voltage. Text label indicates approximate position of the patch-clamp pipette. Red arrows indicate stimulus-sensitive clusters, white arrows indicate stimulus-insensitive clusters. Images are of a single 2-photon excitation optical slice. Left panel is the average fluorescence of the three frames before depolarization while the right panel is the average fluorescence of three frames at 30, 40, and 50 seconds after depolarization. Scale bar is 10 μm. A movie of time-lapse images the experiment can be found in the supplementary materials.

C. Regions of interest used in analysis for panels D, E, and F. Same slice as panel B. ROI 1 contains the apparent plasma membrane of the cell body of the patch-clamped neuron, it was generated by drawing a path tracing the apparent plasma membrane and then expanding to an ROI containing 15 pixels on either side of the path (4.8 μm total width). ROI 2 contains the area 15-45 pixels outside the membrane path (4.8 μm total width). RO1 3 contains the area more than 45 pixels outside of the membrane path. ROI 0 contains the area more than 15 pixels inside the membrane path. Scale bar is 10μm.

D. Fluorescence from each ROI shown in C. Squares represent ROI 0, circles represent ROI 1, upward triangles represent ROI 2 and upside-down triangles represent ROI 3. 0% F/F_{init} (background) was defined as the mean fluorescence of ROI 0 during the experiment. 100% F/F_{init} was defined as the mean fluorescence of ROI 1 during the first six frames, after subtraction of background. Dashed lines represent the average fluorescence of the first six frames of each ROI. The voltage protocol is shown above.

E. Change in fluorescence during 0 mV step for different ROIs in multiple hippocampal slices. ROIs defined by method in panel C. Circles represent mean fluorescence from six frames during 0 mV stimulus, normalized to mean fluorescence from same ROI in six frames before stimulus. Circle color is consistent between ROIs for each hippocampal slice, red circles are slice in panel D. Black bars are mean ± SEM from 3 hippocampal slices.

F. Kinetics of fluorescence change during a 0 mV step from ROI 1 in multiple hippocampal slices. ROI 1 defined by method in panel C. Lines are single exponential fits (Eq.1). $k_{\Delta F}$ =

0.068 ± 0.026 s^{-1} (yellow), 0.068 ± 0.046 s^{-1} (red), and 0.049 ± 0.021 s^{-1} (green). The voltage protocol is shown above.

G. Region of interest used in analysis for panels H, I, and J. Same images as panel C, left image. The shaded ROI was generated by drawing a path tracing the apparent plasma membrane and then expanding to an ROI containing 5 pixels on either side of the path (1.6 µm total width). Numbers indicate puncta that appear as peaks in panel H. Scale bar is 10µm.

H. A plot of the fluorescence intensity along the ROI shown in panel G before (red line) and during (black line) 0 mV stimulus. Numbers above peaks correspond to puncta labeled in panel G. Red line: mean fluorescence intensity during the three frames immediately before the stimulus, normalized to mean intensity of entire ROI, plotted against distance along path. Black line: mean fluorescence intensity during the three frames at 30, 40, and 50 seconds after the 0 mV stimulus began, normalized by the same value as the red line.

I. Kinetics of fluorescence change of individual puncta from panel G. Asterisks indicate mean fluorescence intensity puncta 1 (red), 4 (yellow), and 5 (blue). Lines are single exponential fits (Eq.1). $k_{\Delta F}$ = 0.071 ± 0.029 s^{-1} (red), 0.067 ± 0.025 s^{-1} (yellow) and 0.119 ± 0.056 s^{-1} (blue). Fits to other puncta had errors larger than $k_{\Delta F}$ values. Values are means of all distances within the width at half maximum of each peak, as determined by eye. 100% F/F_{init} was defined as the mean background subtracted fluorescence of the puncta during the six frames before stimuli. The voltage protocol is displayed above. Note that only 3 puncta are shown in this figure, this was because $k_{\Delta F}$ values were excluded for puncta which had fit errors larger than the $k_{\Delta F}$.

J. Comparison of fluorescence change in response to 0 mV stimulus of puncta and inter-puncta regions. The distances before stimulus shown in the red line of panel H that had $F/F_{init} \geq 1$ (above average) were binned separately from distances with $F/F_{init} < 1$. The mean fluorescence of each region during 0 mV stimulus, panel H black line, was compared to the fluorescence before stimulus, panel H red line. Circles indicate values from three independent hippocampal slices, colors indicate same slices as panel E. Black bars are mean ± SEM from the 3 hippocampal slices.

K. Rate of fluorescence change of GxTX-594 after a 0mV stimulus from puncta (as in panel I), ROI 1 (as in panel F) or Kv2.1-CHO (as in Figure 4 B) cells under similar conditions as neurons in hippocampal slices. Kv2.1-CHO cells were recorded from at the same temperature as neurons (30 °C), in the presence of 100 nM GxTX-594, and using neuronal intracellular solution. Kv2.1-CHO measurements were made by airydisk confocal imaging and used normal CHO extracellular solution. Black bars are mean ± SEM from data shown.

MATERIALS AND METHODS

GxTX594 synthesis

The GxTX peptide used was a guangxitoxin-1E variant. GxTX was functionalized at serine 13 and replaced with a spinster thiol cysteine. Methionine 35 was replaced with norleucine to help prevent oxidation. This peptide was synthesized as described (Tilley et al. 2014).

GxTX was labeled with a Texas red derivative (Alexa Fluor 594 C_5 maleimide, ThermoFisher Scientific, 10256, Waltham, MA). To label the peptide, GxTX lyophilisate was brought to 560 μM in 50% ACN + 1 mM Na_2EDTA. 2.43 μL of (1M Tris, pH 6.83), 4 μL of (10 mM of maleimido-fluorophore in DMSO) and 17.9 μL of (560 μM GxTX-Ser 13-Cys) were added to get a final molarity of 100 mM Tris, 1.6 mM fluorophore and 0.412 mM GxTX in 24.33 μL of reaction solution. Reactants were mixed in a 1.5 mL low protein binding polypropylene tube (LoBind, Eppendorf, Hauppauge, NY) and mixed at 1000 RPM, 20°C for 4 hours (Thermomixer R, Eppendorf). After incubation the tube was centrifuged at 845 RCF for 10 minutes at room temperature. A purple pellet was observed post-centrifugation. The supernatant was transferred to a fresh tube and centrifuged at 845 RCF for 10 minutes. After this 2nd centrifugation, no visible pellet was seen. The supernatant injected onto a reverse phase HPLC C_{18} column (Biobasic- 4.6mm RP-C_{18} 5 µm, Thermo Scientific 72105-154630) equilibrated in 20% ACN, 0.1% TFA at 1 mL/min and eluted with a protocol holding in 30% ACN for 2 minutes, increasing to 30% ACN over 1 minute, then increasing ACN at 0.31% per minute. HPLC effluent was monitored by fluorescence and an absorbance array detector. 1 ml fractions were pooled based on fluorescence (280 nm excitation/ 350 nm emission) and absorbance (214 nm, 280 nm and 594 nm). GxTX-594 peptide-fluorophore conjugate eluted at approximately 35% ACN, and mass was confirmed MALDI-TOF mass spectrometry.

Brain slice methods

Hippocampal slice culture preparation and transfection

All experimental procedures were approved by the University of California Davis Institutional Animal Care and Use Committee and were performed in strict accordance with the Guide for the Care and Use of Laboratory Animals of the NIH. Animals were maintained under standard light dark cycles and had ad libitum access to food and water. Organotypic hippocampal slice cultures were prepared from postnatal day 5-7 rats, as described (Stoppini, Buchs, and Muller 1991)and detailed in the video protocol(Opitz-Araya and Barria 2011). DIV15-30 neurons were transfected 2, 4 ,or 6 days before imaging via biolistic gene transfer (160 psi, Helios gene gun, Bio-Rad), as described in the detailed video protocol(Woods and Zito 2008). 10 ug of plasmid was coated to 6-8 mg of 1.6 um gold beads.

Two-photon slice imaging

Image stacks (512*512 pixels, 1 mm Z-steps; 0.035 μm/pixel) were acquired using a custom 2-photon microscope (Olympus LUMPLFLN 60XW/IR2 objective, 60x, 1.0 NA) with two pulsed Ti:sapphire lasers (Mai Tai: Spectra Physics) tuned to 810 nm (for GxTX594 imaging) and 930 nm (for EGFP imaging) and controlled with ScanImage (Pologruto, Sabatini, and Svoboda 2003). After identifying a neuron expressing Kv2.1-GFP, perfusion was stopped and GxTX-594 was added to the static bath solution to a final concentration of 100 nM. After five minutes incubation, perfusion was restarted, leading to wash-out of GxTX-594 from the slice bath. Red and green photons emitted from the sample were collected with two sets of photomultiplier tubes (Hamamatsu R3896).

Whole-cell slice recording

6 to 7 day old organotypic hippocampal slice cultures, that had not been transfected, were transferred to an imaging chamber with recirculating ACSF maintained at 30°C. To hold the slice to the bottom of the chamber, a horseshoe-shaped piece of gold wire was used to weight the membrane holding the slice. ACSF contained (in mM) 127 NaCl, 25 NaHCO3, 25 D-glucose, 2.5 KCl, 1.25 NaH2PO4, 1 MgCl2, 2 CaCl2, 200 nM TTX, pH 7.3 and aerated with 95% O2/ 5% CO2 (~310mOsm). 4 mL of 100nM GxTX-594 in ACSF were used in the circulating bath to allow the toxin to reach the slice and reach the desired concentration of 100 nM throughout the circulating bath. Images were acquired beginning 3 minutes after GxTX-594 was added. Apparent CA1 neurons with GxTX-594 labeling in a Kv2-like pattern were selected for whole cell patch clamp. Voltage clamp was achieved using an Axopatch 200B amplifier (Axon Instruments) controlled with custom software written in Matlab (MathWorks, Inc.). Patch pipettes (5-7 MΩ) were filled with intracellular solution containing (in mM): 135 Cs-methanesulfonate, 10 Na2-phosphocreatine, 3 Na-L-ascorbate, 4 NaCl, 10 HEPES, 4 MgCl2, 4 Na2ATP, 0.4 NaGTP, pH 7.2. Neurons were clamped at -70 mV. Input resistance and holding current were monitored throughout the experiment. Cells were excluded if the pipette series resistance was higher than 25 MΩ or if the holding current exceeded -100 pA. Neurons with a resting membrane potential of -65 +/- 5 mV were selected for imaging experiments. To activate Kv2 channels, a 50 s depolarizing step from -70 mV to 0 mV was given.

Image analysis

Fluorescence images were analyzed using ImageJ 1.47 software (Schneider, Rasband, and Eliceiri 2012) . Regions of interest (ROIs) were selected manually. Fluorescence intensity (F) was background subtracted using mean F of a region lacking cells. For F/F_{init} normalization, F was the mean preceding stimuli, or the max observed intensity in dose response experiments. Time dependence of fluorescence intensity was fit with a single exponential decay (Eq. 1).

$$F = F_o + Ae^{\frac{(t-t_o)}{\tau}} \qquad \text{(Equation 1)}$$

F_o corresponds to initial intensity and t_o corresponds to initial time. The variables *A*, *t* and τ correspond to the amplitude, time and rate constant, respectively. For colocalization analyses the Pearson coefficient was calculated using the JACoP plugin (Bolte and Cordelieres 2006) . Plotting and curve fitting was performed with IgorPro software (Wavemetrics, Portland, OR), which performs nonlinear least-squares fits using a Levenberg-Marquardt algorithm. Standard deviations are reported in text from individual fits. Arithmetic means are reported for intensity measurements. Geometric means are reported for time constants and rates. Error bars indicate standard errors. Statistical comparison was carried out by a Mann-Whitney U test.

CHO cell methods

CHO cell culture and transfection

CHO-K1 (ATCC) and a variant stably transfected with tetracycline inducible rat Kv2.1 construct (Kv2.1 TREx CHO) were cultured as described previously (Tilley et al. 2014). To induce channel expression in the Kv2.1 TREx CHO cells (Trapani and Korn 2003), 1 ug/mL minocycline (Enzo Life Sciences, Farmingdale), prepared in 70% ethanol at 2 mg/mL, was added to the maintenance media to induce K^+ expression. Minocycline was added 40-48 hours before imaging and voltage clamp fluorometry experiments.

Transfections were achieved with Lipofectamine 2000 (Invitrogen, Product Number 11668027, Lot Number 1888663). 1.1 μL of Lipofectamine was diluted, mixed, and incubated in 110 μL of Opti-MEM (Gibco, Product Number 31985-062, Lot Number 1917064) in a 1:100 ratio for 5 minutes at room temperature. Concurrently, 1 μg of plasmid DNA and 110 μL of Opti-MEM were mixed in the same fashion. After incubation, the DNA and Lipofectamine 2000 mixtures were combined, titurated, and allowed to incubate for 20 minutes. Transfection cocktail mixture was added to freshly seeded cells at approximately 40% confluency and allowed to settle at 37°C. The transfection cocktail was added to cells for 4-6 hours before the media was replaced. Rat

Kv2.1-GFP (Antonucci et al. 2001), rat Kv2.2-GFP (Kirmiz, Palacio, et al. 2018)(Kirmiz, Vierra, et al. 2018), rat Kv1.5-GFP (Li et al. 2001), rat Kv4.2-GFP (Shibata et al. 2003), mouse BK-GFP, rat Kv2.1 S586A-GFP (Kirmiz, Palacio, et al. 2018), rat AMIGO-YFP (H I Bishop et al. 2015), Kv Beta 2 (Shibata et al. 2003) and K CHiP2 plasmids were all kind gifts from James Trimmer, University of California, Davis. Identity of constructs were confirmed by sequencing from their CMV promoter.

Confocal imaging

The CHO cell external (CE) solution used for imaging and electrophysiology contained (in mM): 3.5 KCl, 155 NaCl, 10 HEPES, 1.5 $CaCl_2$, 1 $MgCl_2$, adjusted to pH 7.41 with NaOH. Osmolarity was 315 mOsm. When noted, solution was supplemented with either 10 mM glucose (CEG) or 10 mM glucose and 1% BSA (CEGB).

Confocal images were obtained with an inverted confocal system (Zeiss LSM 880 410900-247-075) run by ZEN black v2.1. A Plan Apochromat 63x/1.40 NA Oil immersion DIC objective (Zeiss 420782-9900-799) was used for imaging experiments; a 63x/ 1.2 Water DIC III objective (Zeiss 441777-9970-000) and voltage clamp fluorometry experiments. GFP and YFP were excited with the 488 nm line from an argon laser (3.2 mW at installation) powered at 0.5% unless otherwise noted. GxTX594 was excited with 594 nm helium-neon laser (0.6 mW at installation) powered at 10% unless otherwise noted. WGA-405 was excited with a 405 nm diode laser, (3.5 mW at installation) powered at 1% unless otherwise noted. Temperature inside the microscope housing was 27-30 °C.

In confocal imaging mode, fluorescence was collected with the microscope's 32-channel gallium arsenide phosphide detector array arranged with a diffraction grating to measure 400-700 nm emissions in 9.6 nm bins. Emission bands were 495-550 nm for GFP and YFP, 605-700 nm for GxTX594, and 420-480 nm for WGA-405. Point spread functions were calculated using ZEN black software using emissions from 0.1 μm fluorescent microspheres, prepared on a slide according to manufacturer's instructions (ThermoFisher T7279) and. The point spread functions for confocal images with the 63x/1.40 Oil DIC objective in the X-Y direction were: 228 nm (488 nm excitation) and 316 nm (594 nm excitation).

In Airy disk imaging mode, fluorescence was obtained with a 32-channel gallium arsenide phosphide detector array arranged in a concentric hexagonal pattern (Zeiss Airyscan 410900-

2058-580). Point spread functions were calculated using ZEN black software using emissions 0.1 μm fluorescent microspheres, prepared on a slide according to manufacturer's instructions (ThermoFisher T7279). After deconvolution, the point spread functions for the 63x/1.40 NA Oil DIC objective were: 124 nm in X-Y and 216 nm in Z (488 nm excitation); 168 nm in X-Y and 212 nm in Z (594 nm excitation).

For 63x/1.20 Water DIC III objective after deconvolution, the point spread function for 488 was 187nm in X-Y and 214nm in Z. The PSF for 594 was 210 nm in X-Y and 213 nm in Z.

Prior to imaging, cell maintenance media was removed and replaced with CEGB.

For time-lapse, dose-response experiments, cells were incubated in the microscope chamber with indicated concentrations of GxTX594 for 10 minutes followed by manual wash-out with CEGB solution. 15 minutes after wash-out, GxTX594 was added again at a 10-fold higher concentration. Washout and toxin solutions were added manually via a syringe into a ~100 uL perfusion chamber (Warner Instrument RC-24N). Flow rate was ~1mL/10sec. Images were taken every 5 sec. Laser power was set to 0.5% for the 488 nm laser and 1.5% for the 594 nm laser.

For all other imaging experiments, cells were plated in uncoated 35 mm dishes with an inset No. 1.5 coverslip (MatTek P35G-1.5-20-C).

For colocalization experiments with GFP-tagged proteins, cells were incubated in 100 nM GxTX594 for 5 minutes and then thoroughly washed in CEGB before imaging.

CHO cell voltage clamp fluorometry

Kv2.1-TREx-CHO cells plated in glass bottom 35 mm dishes were washed with CEGB, placed in the microscope, and then incubated with 100 uL of 100 nM GxTX594 for 5 minutes to rapidly load cells. Before patch clamping, the solution was diluted with 1 mL of CEG for a working concentration of 9 nM GxTX594 during experiments. Cells with obvious GxTX594 surface staining were voltage clamped in whole cell mode with a patch clamp amplifier (HEKA EPC-10) run by Patchmaster software (HEKA, Bellmore, NY). The patch pipette contained a potassium-deficient cesium internal pipette solution to limit channel conductance and reduce voltage error: 70 mM CsCl, 50 mM CsF, 35mM NaCl, 1 mM EGTA, 10 mM HEPES, brought to pH 7.4 with CsOH. Osmolarity was 310 mOsm. The calculated liquid junction potential of 3.5 mV was not accounted for. Borosilicate glass pipettes (Sutter BF 150-110-10HP) were pulled with blunt tips to resistances less than 3.0 MΩ in these solutions. Cells were held at -80mV unless noted and stepped to indicated voltages. The voltage step stimulus was held until there was an observed a change in fluorescence. For stimuli frequency dependence experiments, cells were given 2 ms steps to 40 mV at various frequencies (0.02, 5, 10, 20, 50,100,150 or 200 Hz). Images for voltage clamp fluorometry were taken using the Airy-disk detector with the settings described above.

Electrophysiology

Whole cell voltage clamp was used to measure currents from CHO cells transfected with Kv2.1-GFP, Kv2.2-GFP, Kv1.4-GFP, Kv4.2-GFP, BK-GFP or GFP using the methods mentioned above. Cells were plated on glass bottom dishes and media replaced with CEG just before recording. Cells were held at -80 mV, then 100 ms voltage steps were delivered ranging from -80 mV to +80 mV in +5 mV increments. Pulses were repeated every 2 seconds. The external (bath) solution contained CE solution. The internal (pipette) solution contained (in mM): 35 KOH, 70 KCl, 50 KF, 50 HEPES, 5 EGTA adjusted to pH 7.2 with KOH. Liquid junction potential (calculated to be 7.8 mV) was not corrected for. Borosilicate glass pipettes (Sutter Instruments, Cat #BF150-110-10HP) with resistance less that 3 MΩ were used to patch the cells. Recordings were at room temperature (22–24 C). Voltage clamp was achieved with an Axon Axopatch 200B amplifier (MDS Analytical Technologies, Sunnyvale, CA) run by PATCHMASTER software, v2x90.2 (HEKA, Bellmore, NY). Holding potential was -80 mV. Capacitance and Ohmic leak were subtracted using a P/5 protocol. Recordings were low pass filtered at 10 kHz and digitized at 100 kHz. Voltage clamp data were analyzed and plotted with IGORPRO software, version 7 (Wavemetrics, Portland, OR,). Current amplitudes at each voltage were the average from 0.19-0.20 s after voltage step. As the experiments plotted in Figure 6 Supplement 1A were merely to confirm functional expression of ion channels at the cell surface, series resistance compensation was not used and substantial cell voltage errors are predicted to result.

References

Adams, S R. 2010. “How Calcium Indicators Work.” *Cold Spring Harb Protoc* 2010 (3): pdb top70. https://doi.org/10.1101/pdb.top70.

Ahuja, S, S Mukund, L Deng, K Khakh, E Chang, H Ho, S Shriver, et al. 2015. “Structural Basis of Nav1.7 Inhibition by an Isoform-Selective Small-Molecule Antagonist.” *Science* 350 (6267): aac5464. https://doi.org/10.1126/science.aac5464.

Antonucci, D E, S T Lim, S Vassanelli, and J S Trimmer. 2001. “Dynamic Localization and Clustering of Dendritic Kv2.1 Voltage-Dependent Potassium Channels in Developing Hippocampal Neurons.” *Neuroscience* 108 (1): 69–81.

Armstrong, C M, and F Bezanilla. 1973. “Currents Related to Movement of the Gating Particles of the Sodium Channels.” *Nature* 242 (5398): 459–61.

Bestvater, F, E Spiess, G Stobrawa, M Hacker, T Feurer, T Porwol, U Berchner-Pfannschmidt, C Wotzlaw, and H Acker. 2002. “Two-Photon Fluorescence Absorption and Emission Spectra of Dyes Relevant for Cell Imaging.” *J Microsc* 208 (Pt 2): 108–15.

Bezanilla, F. 2018. “Gating Currents.” *J Gen Physiol* 150 (7): 911–32. https://doi.org/10.1085/jgp.201812090.

Bishop, H I, D Guan, E Bocksteins, L K Parajuli, K D Murray, M M Cobb, H Misonou, K Zito, R C Foehring, and J S Trimmer. 2015. “Distinct Cell- and Layer-Specific Expression Patterns and Independent Regulation of Kv2 Channel Subtypes in Cortical Pyramidal Neurons.” *J Neurosci* 35 (44): 14922–42. https://doi.org/10.1523/jneurosci.1897-15.2015.

Bishop, Hannah I, Melanie M Cobb, Michael Kirmiz, Laxmi K Parajuli, Danielle Mandikian, Ashleigh M Philp, Mikhail Melnik, and Juha Kuja-panula. 2018. “Kv2 Ion Channels Determine the Expression and Localization of the Associated AMIGO-1 Cell Adhesion Molecule in Adult Brain Neurons” 11 (January): 1–20. https://doi.org/10.3389/fnmol.2018.00001.

Blaine, J T, and A B Ribera. 2001. “Kv2 Channels Form Delayed-Rectifier Potassium Channels in Situ.” *J Neurosci* 21 (5): 1473–80.

Bolte, S, and F P Cordelieres. 2006. “A Guided Tour into Subcellular Colocalization Analysis in Light Microscopy.” *J Microsc* 224 (Pt 3): 213–32. https://doi.org/10.1111/j.1365-2818.2006.01706.x.

Catterall, W A, S Cestele, V Yarov-Yarovoy, F H Yu, K Konoki, and T Scheuer. 2007. “Voltage-Gated Ion Channels and Gating Modifier Toxins.” *Toxicon* 49 (2): 124–41. https://doi.org/10.1016/j.toxicon.2006.09.022.

Cobb, Melanie M, Daniel C Austin, Jon T Sack, and James S Trimmer. 2015. “Cell Cycle-

Dependent Changes in Localization and Phosphorylation of the Plasma Membrane Kv2 . 1 K ⁒ Channel Impact Endoplasmic Reticulum Membrane Contact Sites In” 290 (49): 29189–201. https://doi.org/10.1074/jbc.M115.690198.

Dockendorff, C, D M Gandhi, I H Kimball, K S Eum, R Rusinova, H I Ingolfsson, R Kapoor, et al. 2018. “Synthetic Analogues of the Snail Toxin 6-Bromo-2-Mercaptotryptamine Dimer (BrMT) Reveal That Lipid Bilayer Perturbation Does Not Underlie Its Modulation of Voltage-Gated Potassium Channels.” *Biochemistry* 57 (18): 2733–43. https://doi.org/10.1021/acs.biochem.8b00292.

Du, J, L L Haak, E Phillips-Tansey, J T Russell, and C J McBain. 2000. “Frequency-Dependent Regulation of Rat Hippocampal Somato-Dendritic Excitability by the K+ Channel Subunit Kv2.1.” *J Physiol* 522 Pt 1: 19–31.

Eichel, K, and M von Zastrow. 2018. “Subcellular Organization of GPCR Signaling.” *Trends Pharmacol Sci* 39 (2): 200–208. https://doi.org/10.1016/j.tips.2017.11.009.

Eyring, Henry. 2004. “The Activated Complex in Chemical Reactions” 107 (November 1934). https://doi.org/10.1063/1.1749604.

Feinshreiber, L, D Singer-Lahat, R Friedrich, U Matti, A Sheinin, O Yizhar, R Nachman, et al. 2010. “Non-Conducting Function of the Kv2.1 Channel Enables It to Recruit Vesicles for Release in Neuroendocrine and Nerve Cells.” *J Cell Sci* 123 (Pt 11): 1940–47. https://doi.org/10.1242/jcs.063719.

Fox, P D, C J Haberkorn, E J Akin, P J Seel, D Krapf, and M M Tamkun. 2015. “Induction of Stable ER-Plasma-Membrane Junctions by Kv2.1 Potassium Channels.” *J Cell Sci* 128 (11): 2096–2105. https://doi.org/10.1242/jcs.166009.

Fox, P D, R J Loftus, and M M Tamkun. 2013. “Regulation of Kv2.1 K(+) Conductance by Cell Surface Channel Density.” *J Neurosci* 33 (3): 1259–70. https://doi.org/10.1523/jneurosci.3008-12.2013.

Fu, J, X Dai, G Plummer, K Suzuki, A Bautista, J M Githaka, L Senior, et al. 2017. “Kv2.1 Clustering Contributes to Insulin Exocytosis and Rescues Human Beta-Cell Dysfunction.” *Diabetes* 66 (7): 1890–1900. https://doi.org/10.2337/db16-1170.

Gilchrist, J, S Das, F Van Petegem, and F Bosmans. 2013. “Crystallographic Insights into Sodium-Channel Modulation by the Beta4 Subunit.” *Proc Natl Acad Sci U S A* 110 (51): E5016-24. https://doi.org/10.1073/pnas.1314557110.

Greitzer-Antes, D, L Xie, T Qin, H Xie, D Zhu, S Dolai, T Liang, et al. 2018. “Kv2.1 Clusters on Beta-Cell Plasma Membrane Act as Reservoirs That Replenish Pools of Newcomer Insulin Granule through Their Interaction with Syntaxin-3.” *J Biol Chem* 293 (18): 6893–6904.

https://doi.org/10.1074/jbc.RA118.002703.

Herrington, J. 2007. "Gating Modifier Peptides as Probes of Pancreatic Beta-Cell Physiology." *Toxicon* 49 (2): 231–38. https://doi.org/10.1016/j.toxicon.2006.09.012.

Herrington, J, Y P Zhou, R M Bugianesi, P M Dulski, Y Feng, V A Warren, M M Smith, et al. 2006. "Blockers of the Delayed-Rectifier Potassium Current in Pancreatic Beta-Cells Enhance Glucose-Dependent Insulin Secretion." *Diabetes* 55 (4): 1034–42.

Irannejad, R, J C Tomshine, J R Tomshine, M Chevalier, J P Mahoney, J Steyaert, S G Rasmussen, et al. 2013. "Conformational Biosensors Reveal GPCR Signalling from Endosomes." *Nature* 495 (7442): 534–38. https://doi.org/10.1038/nature12000.

Islas, L D, and F J Sigworth. 1999. "Voltage Sensitivity and Gating Charge in Shaker and Shab Family Potassium Channels." *J Gen Physiol* 114 (5): 723–42.

———. 2001. "Electrostatics and the Gating Pore of Shaker Potassium Channels." *J Gen Physiol* 117 (1): 69–89.

Jara-Oseguera, A, I G Ishida, G E Rangel-Yescas, N Espinosa-Jalapa, J A Perez-Guzman, D Elias-Vinas, R Le Lagadec, T Rosenbaum, and L D Islas. 2011. "Uncoupling Charge Movement from Channel Opening in Voltage-Gated Potassium Channels by Ruthenium Complexes." *J Biol Chem* 286 (18): 16414–25. https://doi.org/10.1074/jbc.M110.198010.

Johnson, B, A N Leek, L Sole, E E Maverick, T P Levine, and M M Tamkun. 2018. "Kv2 Potassium Channels Form Endoplasmic Reticulum/Plasma Membrane Junctions via Interaction with VAPA and VAPB." *Proc Natl Acad Sci U S A* 115 (31): E7331–40. https://doi.org/10.1073/pnas.1805757115.

Kirmiz, M, S Palacio, P Thapa, A N King, J T Sack, and J S Trimmer. 2018. "Remodeling Neuronal ER-PM Junctions Is a Conserved Nonconducting Function of Kv2 Plasma Membrane Ion Channels." *Mol Biol Cell* 29 (20): mbcE18050337. https://doi.org/10.1091/mbc.E18-05-0337.

Kirmiz, M, N C Vierra, S Palacio, and J S Trimmer. 2018. "Identification of VAPA and VAPB as Kv2 Channel-Interacting Proteins Defining Endoplasmic Reticulum-Plasma Membrane Junctions in Mammalian Brain Neurons." *J Neurosci*. https://doi.org/10.1523/jneurosci.0893-18.2018.

Koide, A, S Abbatiello, L Rothgery, and S Koide. 2002. "Probing Protein Conformational Changes in Living Cells by Using Designer Binding Proteins: Application to the Estrogen Receptor." *Proc Natl Acad Sci U S A* 99 (3): 1253–58. https://doi.org/10.1073/pnas.032665299.

Lewis, G N. 1925. "A New Principle of Equilibrium." *Proc Natl Acad Sci U S A* 11 (3): 179–83.

Li, H, W Guo, H Xu, R Hood, A T Benedict, and J M Nerbonne. 2001. “Functional Expression of a GFP-Tagged Kv1.5 Alpha-Subunit in Mouse Ventricle.” *Am J Physiol Heart Circ Physiol* 281 (5): H1955-67. https://doi.org/10.1152/ajpheart.2001.281.5.H1955.

Liu, P W, and B P Bean. 2014. “Kv2 Channel Regulation of Action Potential Repolarization and Firing Patterns in Superior Cervical Ganglion Neurons and Hippocampal CA1 Pyramidal Neurons.” *J Neurosci* 34 (14): 4991–5002. https://doi.org/10.1523/jneurosci.1925-13.2014.

Long, S B, E B Campbell, and R Mackinnon. 2005. “Voltage Sensor of Kv1.2: Structural Basis of Electromechanical Coupling.” *Science* 309 (5736): 903–8. https://doi.org/10.1126/science.1116270.

MacDonald, P E, A M Salapatek, and M B Wheeler. 2003. “Temperature and Redox State Dependence of Native Kv2.1 Currents in Rat Pancreatic Beta-Cells.” *J Physiol* 546 (Pt 3): 647–53.

Maffie, J K, E Dvoretskova, P E Bougis, M F Martin-Eauclaire, and B Rudy. 2013. “Dipeptidyl-Peptidase-like-Proteins Confer High Sensitivity to the Scorpion Toxin AmmTX3 to Kv4-Mediated A-Type K+ Channels.” *J Physiol* 591 (10): 2419–27. https://doi.org/10.1113/jphysiol.2012.248831.

Mandikian, D, E Bocksteins, L K Parajuli, H I Bishop, O Cerda, R Shigemoto, and J S Trimmer. 2014. “Cell Type-Specific Spatial and Functional Coupling between Mammalian Brain Kv2.1 K+ Channels and Ryanodine Receptors.” *J Comp Neurol* 522 (15): 3555–74. https://doi.org/10.1002/cne.23641.

Mann, V R, A S Powers, D C Tilley, J T Sack, and B E Cohen. 2018. “Azide-Alkyne Click Conjugation on Quantum Dots by Selective Copper Coordination.” *ACS Nano* 12 (5): 4469–77. https://doi.org/10.1021/acsnano.8b00575.

Mannuzzu, L M, M M Moronne, and E Y Isacoff. 1996. “Direct Physical Measure of Conformational Rearrangement Underlying Potassium Channel Gating.” *Science* 271 (5246): 213–16.

McCormack, K, S Santos, M L Chapman, D S Krafte, B E Marron, C W West, M J Krambis, et al. 2013. “Voltage Sensor Interaction Site for Selective Small Molecule Inhibitors of Voltage-Gated Sodium Channels.” *Proc Natl Acad Sci U S A* 110 (29): E2724-32. https://doi.org/10.1073/pnas.1220844110.

Misonou, H, M Menegola, D P Mohapatra, L K Guy, K S Park, and J S Trimmer. 2006. “Bidirectional Activity-Dependent Regulation of Neuronal Ion Channel Phosphorylation.” *J Neurosci* 26 (52): 13505–14. https://doi.org/10.1523/jneurosci.3970-06.2006.

Misonou, H, D P Mohapatra, M Menegola, and J S Trimmer. 2005. “Calcium- and Metabolic

State-Dependent Modulation of the Voltage-Dependent Kv2.1 Channel Regulates Neuronal Excitability in Response to Ischemia.” *J Neurosci* 25 (48): 11184–93. https://doi.org/10.1523/jneurosci.3370-05.2005.

Murakoshi, H, G Shi, R H Scannevin, and J S Trimmer. 1997. “Phosphorylation of the Kv2.1 K+ Channel Alters Voltage-Dependent Activation.” *Mol Pharmacol* 52 (5): 821–28.

O’Connell, K M, R Loftus, and M M Tamkun. 2010. “Localization-Dependent Activity of the Kv2.1 Delayed-Rectifier K+ Channel.” *Proc Natl Acad Sci U S A* 107 (27): 12351–56. https://doi.org/10.1073/pnas.1003028107.

Opitz-Araya, X, and A Barria. 2011. “Organotypic Hippocampal Slice Cultures.” *J Vis Exp*, no. 48. https://doi.org/10.3791/2462.

Palacio, S, V Chevaleyre, D H Brann, K D Murray, R A Piskorowski, and J S Trimmer. 2017. “Heterogeneity in Kv2 Channel Expression Shapes Action Potential Characteristics and Firing Patterns in CA1 versus CA2 Hippocampal Pyramidal Neurons.” *ENeuro* 4 (4). https://doi.org/10.1523/eneuro.0267-17.2017.

Peltola, M A, J Kuja-Panula, S E Lauri, T Taira, and H Rauvala. 2011. “AMIGO Is an Auxiliary Subunit of the Kv2.1 Potassium Channel.” *EMBO Rep* 12 (12): 1293–99. https://doi.org/10.1038/embor.2011.204.

Peretz, A, L Pell, Y Gofman, Y Haitin, L Shamgar, E Patrich, P Kornilov, O Gourgy-Hacohen, N Ben-Tal, and B Attali. 2010. “Targeting the Voltage Sensor of Kv7.2 Voltage-Gated K+ Channels with a New Gating-Modifier.” *Proc Natl Acad Sci U S A* 107 (35): 15637–42. https://doi.org/10.1073/pnas.0911294107.

Plant, L D, E J Dowdell, I S Dementieva, J D Marks, and S A Goldstein. 2011. “SUMO Modification of Cell Surface Kv2.1 Potassium Channels Regulates the Activity of Rat Hippocampal Neurons.” *J Gen Physiol* 137 (5): 441–54. https://doi.org/10.1085/jgp.201110604.

Pologruto, T A, B L Sabatini, and K Svoboda. 2003. “ScanImage: Flexible Software for Operating Laser Scanning Microscopes.” *Biomed Eng Online* 2: 13. https://doi.org/10.1186/1475-925x-2-13.

Redman, P T, K He, K A Hartnett, B S Jefferson, L Hu, P A Rosenberg, E S Levitan, and E Aizenman. 2007. “Apoptotic Surge of Potassium Currents Is Mediated by P38 Phosphorylation of Kv2.1.” *Proc Natl Acad Sci U S A* 104 (9): 3568–73. https://doi.org/10.1073/pnas.0610159104.

Rios, E, and G Brum. 1987. “Involvement of Dihydropyridine Receptors in Excitation-Contraction Coupling in Skeletal Muscle.” *Nature* 325 (6106): 717–20.

https://doi.org/10.1038/325717a0.

Sack, J T, R W Aldrich, and W F Gilly. 2004. “A Gastropod Toxin Selectively Slows Early Transitions in the Shaker K Channel’s Activation Pathway.” *J Gen Physiol* 123 (6): 685–96. https://doi.org/10.1085/jgp.200409047.

Sack, J T, N Stephanopoulos, D C Austin, M B Francis, and J S Trimmer. 2013. “Antibody-Guided Photoablation of Voltage-Gated Potassium Currents.” *J Gen Physiol* 142 (3): 315–24. https://doi.org/10.1085/jgp.201311023.

Schmalhofer, W A, K S Ratliff, A Weinglass, G J Kaczorowski, M L Garcia, and J Herrington. 2009. “A KV2.1 Gating Modifier Binding Assay Suitable for High Throughput Screening.” *Channels (Austin)* 3 (6): 437–47.

Schneider, C A, W S Rasband, and K W Eliceiri. 2012. “NIH Image to ImageJ: 25 Years of Image Analysis.” *Nat Methods* 9 (7): 671–75.

Schneider, M F, and W K Chandler. 1973. “Voltage Dependent Charge Movement of Skeletal Muscle: A Possible Step in Excitation-Contraction Coupling.” *Nature* 242 (5395): 244–46.

Scholle, A, S Dugarmaa, T Zimmer, M Leonhardt, R Koopmann, B Engeland, O Pongs, and K Benndorf. 2004. “Rate-Limiting Reactions Determining Different Activation Kinetics of Kv1.2 and Kv2.1 Channels.” *J Membr Biol* 198 (2): 103–12. https://doi.org/10.1007/s00232-004-0664-0.

Seoh, S A, D Sigg, D M Papazian, and F Bezanilla. 1996. “Voltage-Sensing Residues in the S2 and S4 Segments of the Shaker K+ Channel.” *Neuron* 16 (6): 1159–67.

Shi, G, K Nakahira, S Hammond, K J Rhodes, L E Schechter, and J S Trimmer. 1996. “Beta Subunits Promote K+ Channel Surface Expression through Effects Early in Biosynthesis.” *Neuron* 16 (4): 843–52.

Shibata, R, H Misonou, C R Campomanes, A E Anderson, L A Schrader, L C Doliveira, K I Carroll, J D Sweatt, K J Rhodes, and J S Trimmer. 2003. “A Fundamental Role for KChIPs in Determining the Molecular Properties and Trafficking of Kv4.2 Potassium Channels.” *J Biol Chem* 278 (38): 36445–54. https://doi.org/10.1074/jbc.M306142200.

Siegel, M S, and E Y Isacoff. 1997. “A Genetically Encoded Optical Probe of Membrane Voltage.” *Neuron* 19 (4): 735–41.

Singer-Lahat, D, D Chikvashvili, and I Lotan. 2008. “Direct Interaction of Endogenous Kv Channels with Syntaxin Enhances Exocytosis by Neuroendocrine Cells.” *PLoS One* 3 (1): e1381. https://doi.org/10.1371/journal.pone.0001381.

Speca, D J, G Ogata, D Mandikian, H I Bishop, S W Wiler, K Eum, H J Wenzel, et al. 2014. “Deletion of the Kv2.1 Delayed Rectifier Potassium Channel Leads to Neuronal and

Behavioral Hyperexcitability.” *Genes Brain Behav* 13 (4): 394–408. https://doi.org/10.1111/gbb.12120.

Stoppini, L, P A Buchs, and D Muller. 1991. “A Simple Method for Organotypic Cultures of Nervous Tissue.” *J Neurosci Methods* 37 (2): 173–82.

Tanabe, T, K G Beam, J A Powell, and S Numa. 1988. “Restoration of Excitation-Contraction Coupling and Slow Calcium Current in Dysgenic Muscle by Dihydropyridine Receptor Complementary DNA.” *Nature* 336 (6195): 134–39. https://doi.org/10.1038/336134a0.

Tao, X, A Lee, W Limapichat, D A Dougherty, and R MacKinnon. 2010. “A Gating Charge Transfer Center in Voltage Sensors.” *Science* 328 (5974): 67–73. https://doi.org/10.1126/science.1185954.

Tilley, D C, J M Angueyra, K S Eum, H Kim, L H Chao, A W Peng, and J T Sack. 2018. “The Tarantula Toxin GxTx Detains K(+) Channel Gating Charges in Their Resting Conformation.” *J Gen Physiol*. https://doi.org/10.1085/jgp.201812213.

Tilley, D C, K S Eum, S Fletcher-Taylor, D C Austin, C Dupre, L A Patron, R L Garcia, et al. 2014. “Chemoselective Tarantula Toxins Report Voltage Activation of Wild-Type Ion Channels in Live Cells.” *Proc Natl Acad Sci U S A* 111 (44): E4789-96. https://doi.org/10.1073/pnas.1406876111.

Trapani, J G, and S J Korn. 2003. “Control of Ion Channel Expression for Patch Clamp Recordings Using an Inducible Expression System in Mammalian Cell Lines.” *BMC Neurosci* 4: 15. https://doi.org/10.1186/1471-2202-4-15.

Tsvetanova, N G, R Irannejad, and M von Zastrow. 2015. “G Protein-Coupled Receptor (GPCR) Signaling via Heterotrimeric G Proteins from Endosomes.” *J Biol Chem* 290 (11): 6689–96. https://doi.org/10.1074/jbc.R114.617951.

Woods, G, and K Zito. 2008. “Preparation of Gene Gun Bullets and Biolistic Transfection of Neurons in Slice Culture.” *J Vis Exp*, no. 12. https://doi.org/10.3791/675.

Yang, F, and J Zheng. 2014. “High Temperature Sensitivity Is Intrinsic to Voltage-Gated Potassium Channels.” *Elife* 3: e03255. https://doi.org/10.7554/eLife.03255.

Yang, W, and R Yuste. 2017. “In Vivo Imaging of Neural Activity.” *Nat Methods* 14 (4): 349–59. https://doi.org/10.1038/nmeth.4230.

Yu, M, S L Liu, P B Sun, H Pan, C L Tian, and L H Zhang. 2016. “Peptide Toxins and Small-Molecule Blockers of BK Channels.” *Acta Pharmacol Sin* 37 (1): 56–66. https://doi.org/10.1038/aps.2015.139.

Zagotta, W N, T Hoshi, and R W Aldrich. 1994. “Shaker Potassium Channel Gating. III: Evaluation of Kinetic Models for Activation.” *J Gen Physiol* 103 (2): 321–62.

Zagotta, W N, T Hoshi, J Dittman, and R W Aldrich. 1994. “Shaker Potassium Channel Gating. II: Transitions in the Activation Pathway.” *J Gen Physiol* 103 (2): 279–319.

Zhang, A H, G Sharma, E A B Undheim, X Jia, and M Mobli. 2018. “A Complicated Complex: Ion Channels, Voltage Sensing, Cell Membranes and Peptide Inhibitors.” *Neurosci Lett* 679: 35–47. https://doi.org/10.1016/j.neulet.2018.04.030.

Zheng, Jie, and Matthew C. Trudeau, eds. n.d. *Handbook of Ion Channels*. 1st ed. CRC Press.

Figure 1

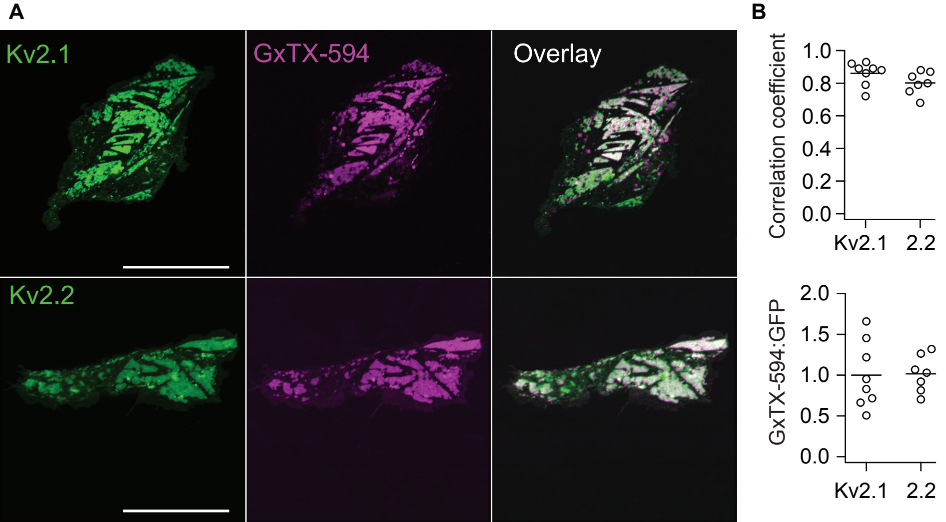
A
B
Kv2.1
GxTX-594
Overlay
Kv2.2
Correlation coefficient
1.0
0.8
0.6
0.4
0.2
0.0
Kv2.1
2.2
GxTX-594:GFP
2.0
1.5
1.0
0.5
0.0
Kv2.1
2.2

Figure 1 S1

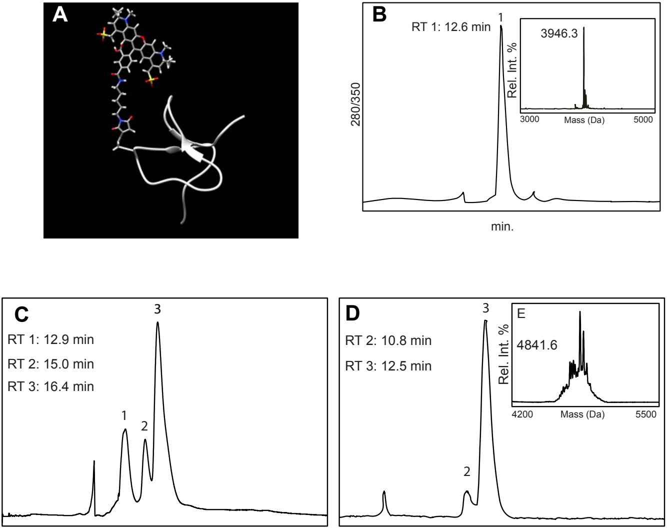
A
B
RT 1: 12.6 min
1
3946.3
Rel. Int. %
3000
Mass (Da)
5000
280/350
min.
C
RT 1: 12.9 min
RT 2: 15.0 min
RT 3: 16.4 min
1
2
3
D
RT 2: 10.8 min
RT 3: 12.5 min
2
3
E
4841.6
Rel. Int. %
4200
Mass (Da)
5500

Figure 2

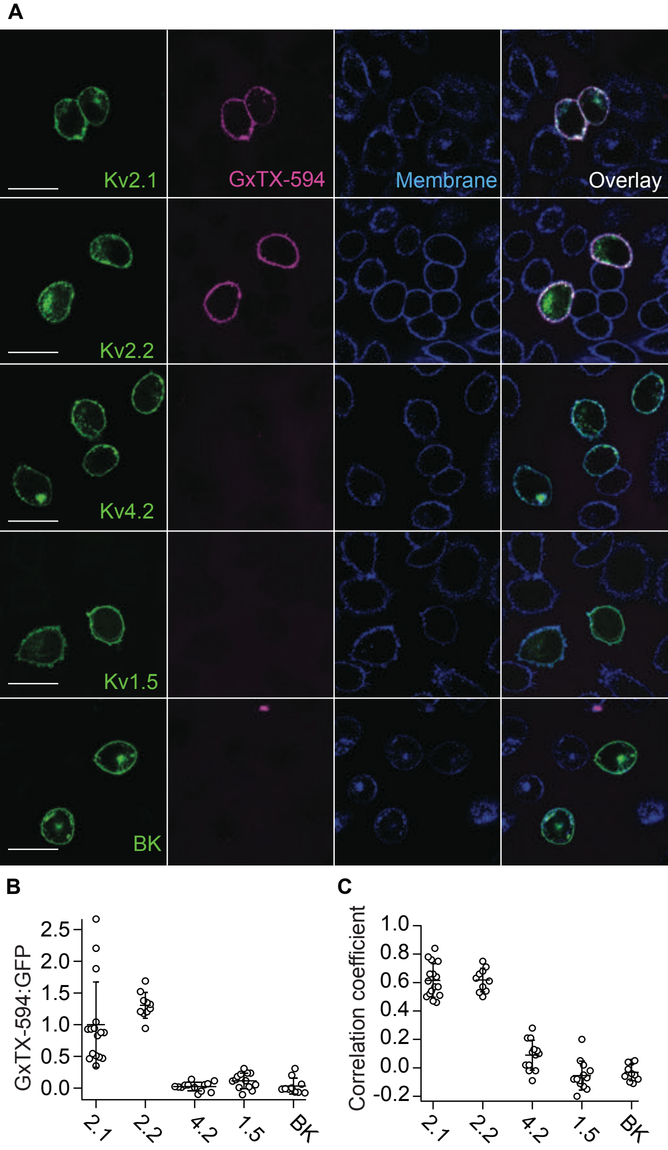
A
Kv2.1
GxTX-594
Membrane
Overlay
Kv2.2
Kv4.2
Kv1.5
BK
B
GxTX-594:GFP
0.0
0.5
1.0
1.5
2.0
2.5
2.1
2.2
4.2
1.5
BK
C
Correlation coefficient
-0.2
0.0
0.2
0.4
0.6
0.8
1.0
2.1
2.2
4.2
1.5
BK

Figure 2 Supplement 1

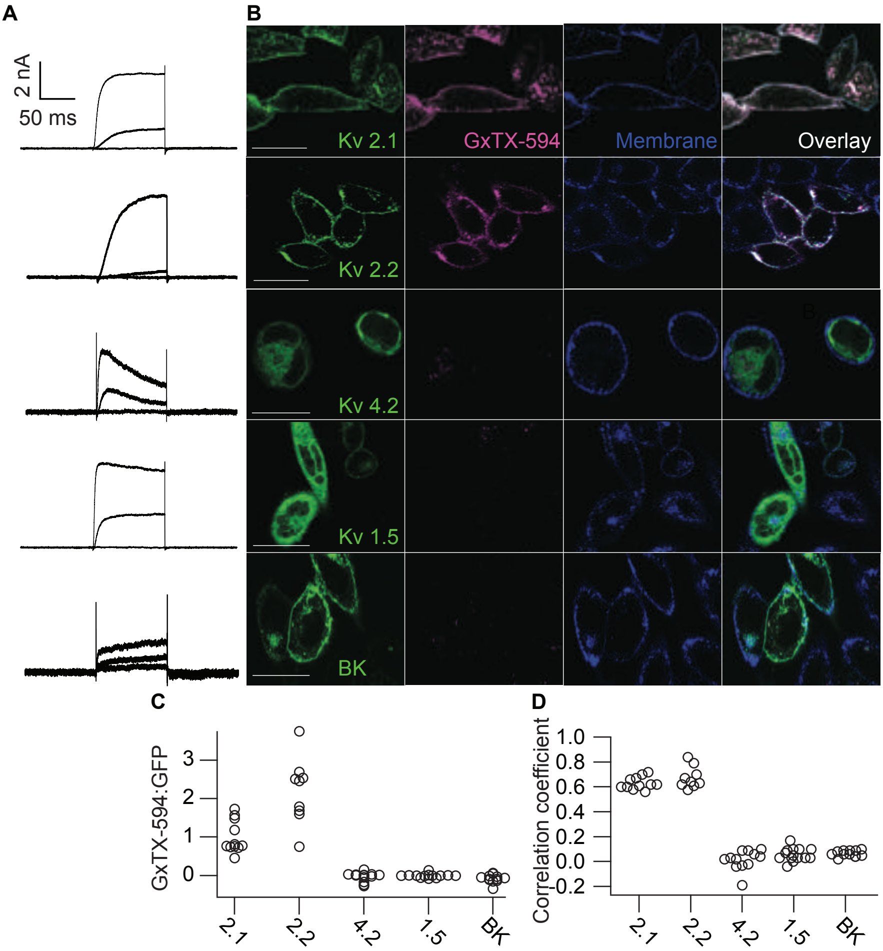

Figure 3

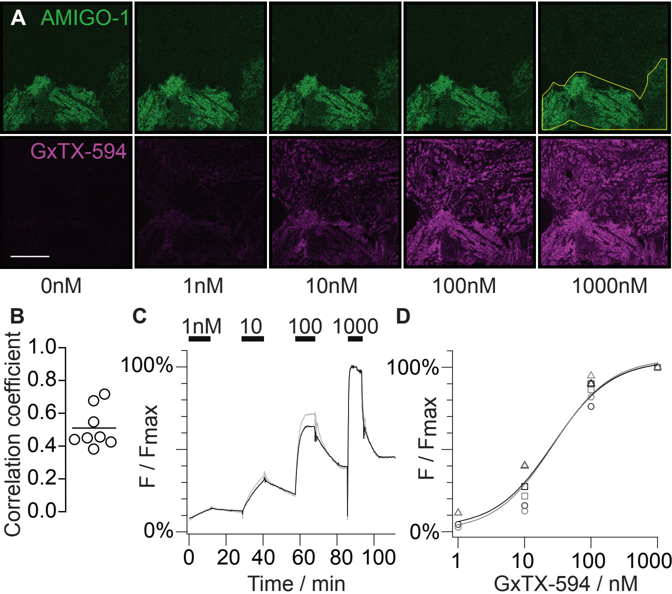
A
AMIGO-1
GxTX-594
0nM
1nM
10nM
100nM
1000nM
B
Correlation coefficient
1.0
0.8
0.6
0.4
0.2
0.0
C
1nM
10
100
1000
100%
0%
F / Fmax
0
20
40
60
80
100
Time / min
D
100%
0%
F / Fmax
1
10
100
1000
GxTX-594 / nM

Figure 4

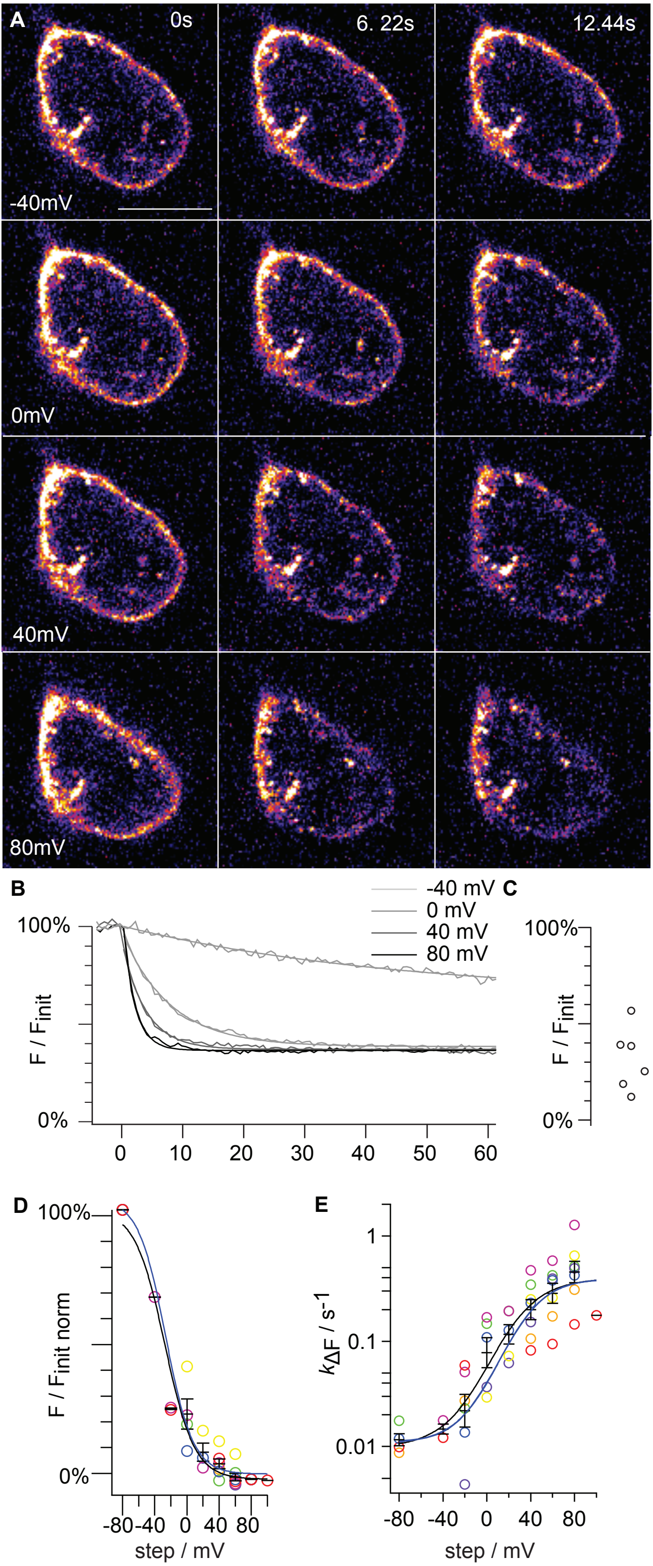
A
0s
6. 22s
12.44s
-40mV
0mV
40mV
80mV
B
-40 mV
0 mV
40 mV
80 mV
100%
0%
F / F_init
0
10
20
30
40
50
60
C
100%
0%
F / F_init
D
100%
0%
F / F_init norm
-80
-40
0
40
80
step / mV
E
1
0.1
0.01
k_ΔF / s^-1
-80
-40
0
40
80
step / mV

Figure 4 Supplement 1

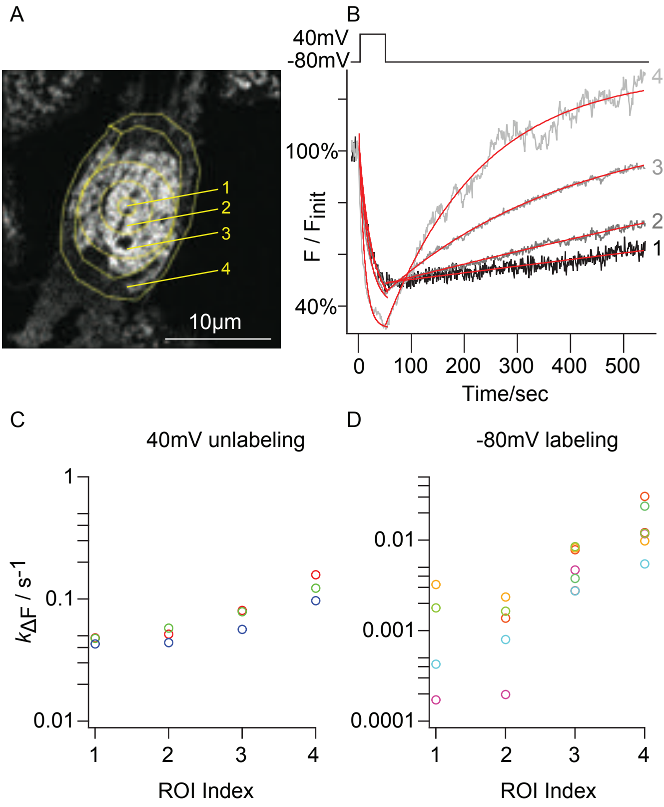

Figure 4 Supplement 2

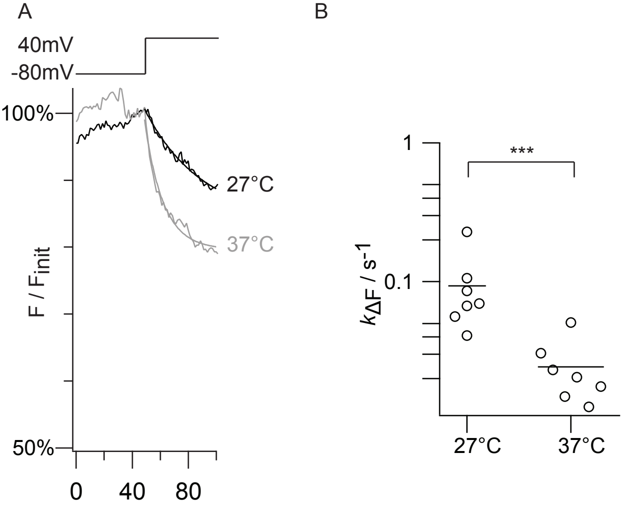

Figure 5

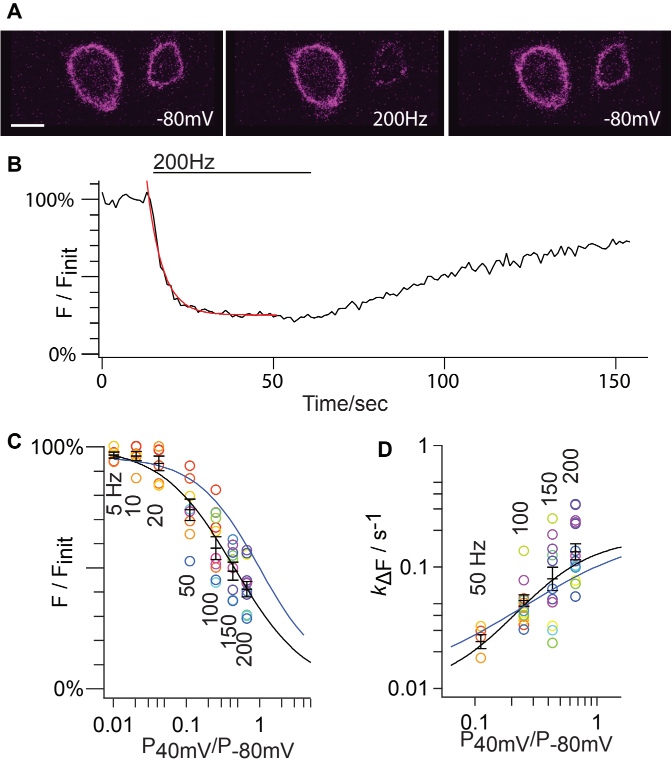
A
-80mV
200Hz
-80mV
B
200Hz
100%
F / F_{init}
0%
0
50
100
150
Time/sec
C
100%
F / F_{init}
0%
5 Hz
10
20
50
100
150
200
0.01
0.1
1
P_{40mV}/P_{-80mV}
D
1
0.1
0.01
$k_{\Delta F}$ / s^{-1}
50 Hz
100
150
200
0.1
1
P_{40mV}/P_{-80mV}

Figure 6

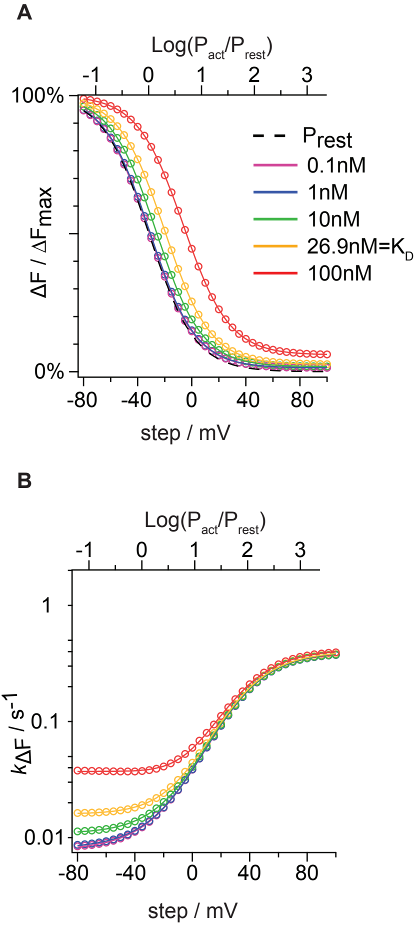
A
Log(P_{act}/P_{rest})
-1
0
1
2
3
100%
0%
ΔF / ΔF$_{max}$
P_{rest}
0.1nM
1nM
10nM
26.9nM=K_D
100nM
-80
-40
0
40
80
step / mV
B
Log(P_{act}/P_{rest})
-1
0
1
2
3
1
0.1
0.01
$k_{\Delta F}$ / s^{-1}
-80
-40
0
40
80
step / mV

Figure 7

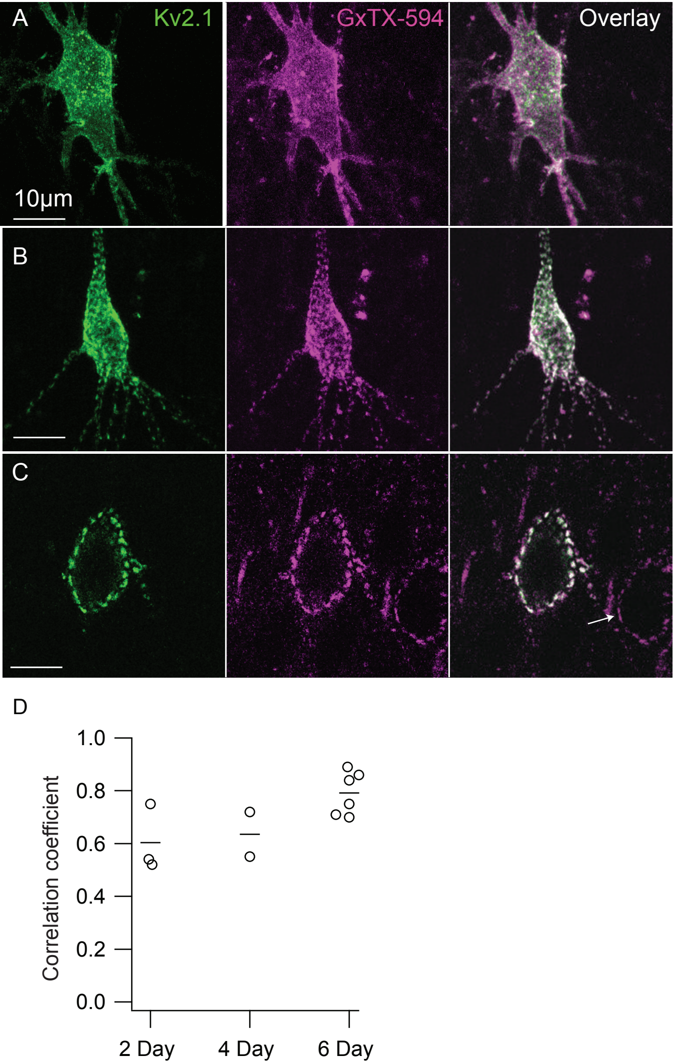
A
Kv2.1
GxTX-594
Overlay
10μm
B
C
D
1.0
0.8
0.6
0.4
0.2
0.0
Correlation coefficient
2 Day
4 Day
6 Day

Figure 7 Supplement 1

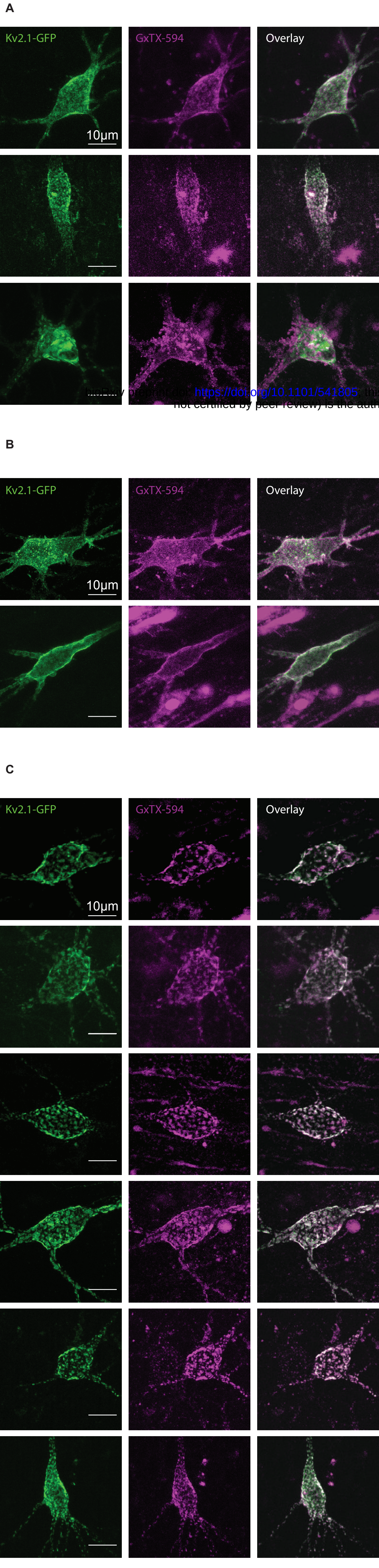

Figure 8

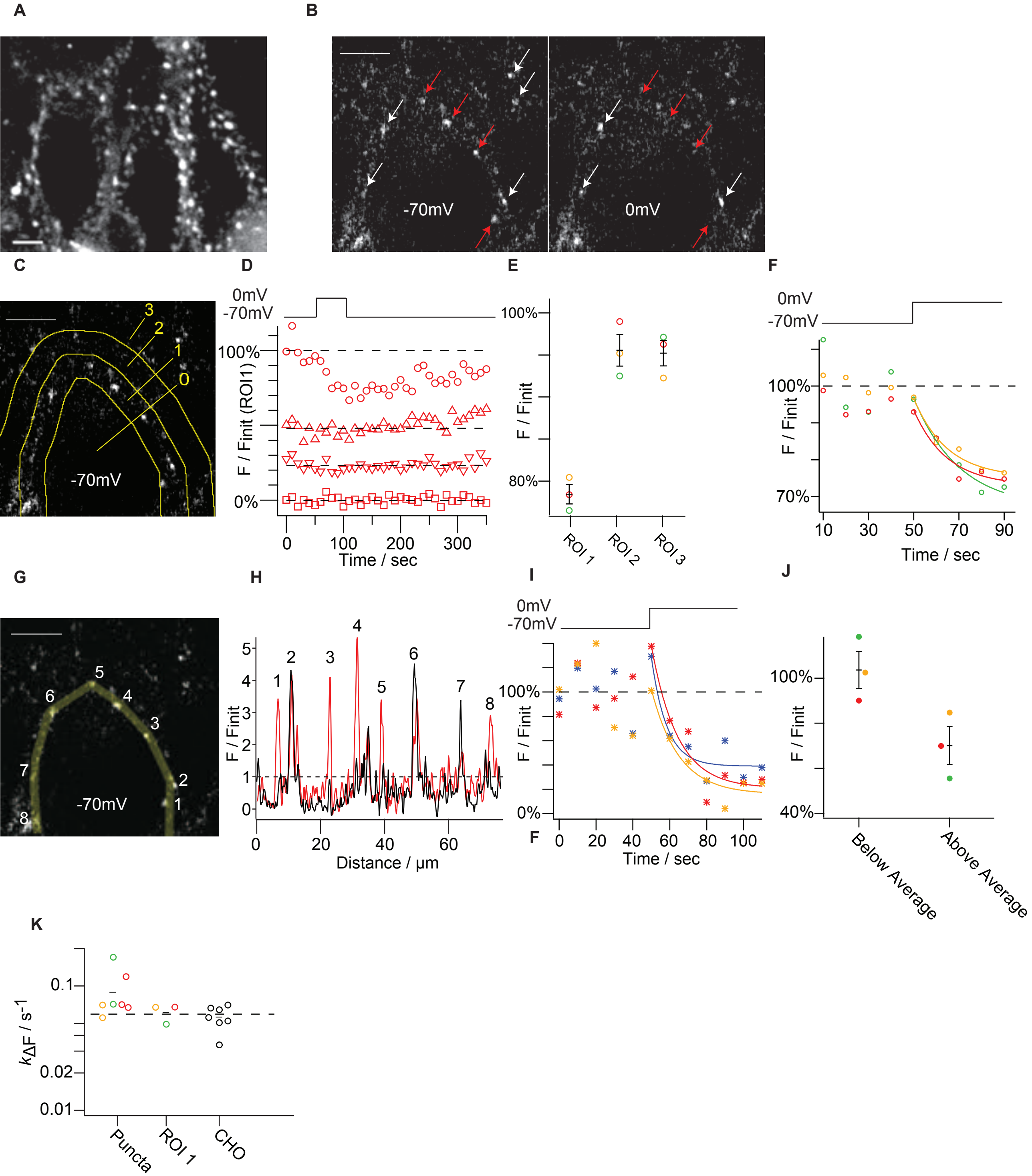
A
B
-70mV
0mV
C
3
2
1
0
-70mV
D
0mV
-70mV
100%
0%
F / Finit (ROI1)
0
100
200
300
Time / sec
E
100%
80%
F / Finit
ROI 1
ROI 2
ROI 3
F
0mV
-70mV
100%
70%
F / Finit
10
30
50
70
90
Time / sec
G
5
6
4
3
7
2
1
8
-70mV
H
5
4
3
2
1
0
F / Finit
1
2
3
4
5
6
7
8
0
20
40
60
Distance / µm
I
0mV
-70mV
100%
0%
F / Finit
0
20
40
60
80
100
Time / sec
F
J
100%
40%
F / Finit
Below Average
Above Average
K
0.1
0.02
0.01
$k_{\Delta F}$ / s^{-1}
Puncta
ROI 1
CHO

Scheme A

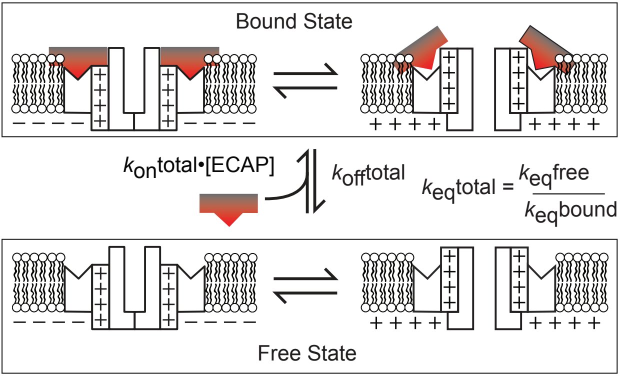

Scheme B